Effect of calcination temperatures on the band gap of Bismuth Ferrite ($BiFeO_3$) – A First Principle Study

Dissertation submitted in partial fulfillment for the
Requirement of the award of the degree of

MASTER OF SCIENCE
IN
PHYSICS

Under the supervision of
Dr. Poonam Uniyal
(Assistant Professor)

Submitted by
Manish Verma
Roll no: - 301304005

School of Physics and Materials Science
Thapar University
Patiala (Punjab) – 147004
July, 2015

Dedicated to the Lord Shri Sai Baba, Shirdi

&

To my Parents and younger Brother

CERTIFICATE

This is to certify that Mr. Manish Verma has worked on this thesis report entitled "Effect of calcination temperatures on the band gap of Bismuth ferrite (BiFeO3) – A first principle study" in partial fulfilment of the requirement for the award of degree of Master of Science in Physics at Thapar University, Patiala. This report is an authentic record of his own work carried out under the supervision of Dr. Poonam Uniyal. The matter embodied in this report is one of the candidate's own record and has not been submitted to any other educational institution in any part or full form for the award of similar kind of degree.

Dr. Poonam Uniyal
(Assistant Professor)
School of Physics and Materials Science
Thapar University, Patiala
INDIA – 147004

Countersigned By:

Dr. Manoj K Sharma
Professor and Head
School of Physics and Materials Science
Thapar University, Patiala
INDIA-147004

Dr. S.S Bhatia
Professor and Dean of Academic affairs
Thapar University, Patiala
INDIA-147004

ABSTRACT

In the present thesis, effect of calcination temperatures on the band gap of $BiFeO_3$ is reported. DFT calculations were performed using GGA+U methodology in the TB-LMTO-ASA code version 47. The ground state electronic properties of $BiFeO_3$ were calculated using the combination of U = 6eV and J =1eV for the Hubbard parameters while keeping the spins of two Fe atoms (Fe1 and Fe2) in the opposite spin directions in the 10 atoms unit cell of $BiFeO_3$, which confirmed the value of band gaps and the nature of band gaps obtained experimentally at two calcination temperatures i.e. 500°C and 600°C. After, the SCF calculations were performed using the rietveld refinement data for the ground state (R3c) $BiFeO_3$ calcined at 500°C and 600°C, equal electronic band structure diagrams were obtained in the two spin directions. Also, the equal partial density of states plots were obtained for oxygen as well as bismuth in contrast with different partial density of states plots for Fe1 and Fe2 atoms in the two spin directions thereby authenticating the anti-ferromagnetism in case of bulk $BiFeO_3$ at both the calcination temperatures of 500°C and 600°C, respectively. Also, the direct band gap values of 2.25eV and 2.16eV were obtained from the TDOS (including both spin1 and 2 directions) closely approximates both the experimental direct band gap values of 2.16eV and 2.25eV at 500°C and 600°C, respectively. Lastly the charge density plot was calculated in a plane to study the nature of chemical bonding among the constituent atoms of $BiFeO_3$ through which it was concluded that the chemical bonding between the Fe and O atoms is not completely ionic with partially directional covalent bonding thrown in it thereby indicating the non-Centro symmetric setup leading to Ferro electricity observed in case of bulk $BiFeO_3$.

ACKNOWLEDGMENTS

My deepest gratitude is to my advisor, Dr. Poonam Uniyal, Assistant Professor, School of Physics and Materials Science, Thapar University, Patiala. I have been amazingly fortunate to have an advisor like her who gave me the freedom to explore on my own and at the same time the guidance to recover when my steps faltered. She taught me how to question thoughts and express ideas. Her patience and support helped me overcome many crisis situations and finish this dissertation. I also specially want to thank Dr. Manoj K. Sharma (HOD - SPMS,Thapar University) without whose support i would not have been able to complete my work in time. I am also thankful to the research scholar of my lab Mr. Piyush Sharma who helped me correcting this thesis. I would like to acknowledge Professor Ole K Anderson's group at Max Planck Institute, Stuttgart, Germany who allowed me to use their code (TB-LMTO-ASA Version 47) for my work. I would also like to acknowledge Dr. Yoshiro K Nohara at Max Planck Institute, Stuttgart, Germany who helped me immensely to complete this work. His patience with handling the errors, suggestions to improve the results and initial helps in installation of the code made it possible for me to complete this work. His quick and timely responses were immensely fruitful for my work. I also thank him for calculating a very important parameter required in my work (Spin- Orbit interaction energy) which was not possible for me to calculate with the type of computational facility at my side. I am also indebted to my father Dr Kanik Ram, Scientist (DRDO) who constantly guided me in my work and also gave me useful advices for improving my work. I am highly thankful to him, to my mother Smt. Purnima Singh and to my younger brother Ankit Verma who always stood by my side during my bad times and always showered their blessings on me. I would like to thank my friends Harsh Sachdev, Ashutosh Mishra, Anurag Tiwari, Ashish Chaudhary, Aayush Gupta, Ashish Pathak, Ankit Kumar and Shivkumar. Lastly, i want to thank from the depth of my heart to the Lord Shri Sai Baba, Shirdi who is the source of inspiration in my life and always showed me the right path to proceed and also took me out from the dark phases of my life till now.

Manish Verma

LIST OF FIGURES AND TABLES

GLOSSARY OF SYMBOLS

t	Tolerance factor
r	ionic radius
χ	Susceptibility of the material
C	Curie constant
T	Temperature
T_N	Neël temperature
H	Magnetic field
M	Magnetization
M_S	Saturation magnetization
M_R	Remnant magnetization
H_C	Coercive field
E	Electric field
E_C	Coercive field
P_r	Remnant polarization
P	Polarization
F	Free energy

ϵ	Dielectric permittivity
μ	Magnetic permeability
P_i^S	Electrical polarization
α_{ij}	Magnetoelectric coupling
μ_B	Bohr magneton
DFT	Density functional theory
LDA	Linear density approximation
GGA	Generalized gradient approximation
U	Hubbard parameter
$\boldsymbol{H}$	Hamiltonian
$\boldsymbol{\nabla}^2$	Laplacian operator
R_I	Nuclear position
M_I	Nuclear mass
r_i	Electronic position
m_i	Electronic mass
Z_I	Atomic mass

$H_{k\text{-}s}$	Kohn sham Hamiltonian
$V_{K\text{-}S}$	Kohn sham potential
F [n(r)]	Universal functional
T [n(r)]	Kinetic energy term
$E_{hartree}$ [n(r)]	Energy due to electrostatic interaction of electrons
E_{xc} [n(r)]	Exchange correlation energy
LSDA	Linear spin density approximation
TDOS	Total density of states
PDOS	Partial density of states

CONTENTS

Chapter-1

Introduction

Introduction

1.1 Multiferroic materials

These are the class of materials which embodies two or more primary ferroic order parameters i.e. ferroelectricity, ferromagnetism, ferrotoroidicity and ferroelasticity. Nowadays, the theory of multiferroism has been expanded to include antiferromagnetic ordering and ferrotoroidicity [1]. In the case of normal ferroic materials, polarization (*P*) is controlled by the electric field (*E*), the magnetization (*M*) is controlled by the magnetic field (*H*). In these materials, there is also a possibility of coupling between the electric and magnetic orders by virtue of which magnetization is induced in the sample with the application of electric field and electric polarization is produced by means of magnetic field. This coupling is known as the magnetoelectric effect as shown below in fig. 1.1.

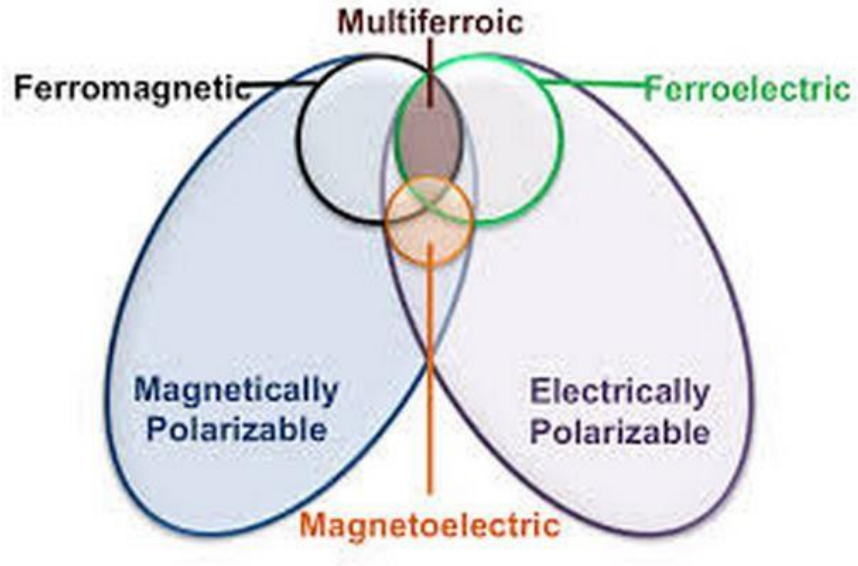

Fig. 1.1: Venn diagram for Multiferroic materials

1.2 Primary ferroic properties

1.2.1 Ferromagnetism

It is the property by virtue of which materials show a stable spontaneous magnetization that can be hysterically switched by an applied magnetic field. It is caused due to automatic allineation of atomic magnetic moments in one particular direction giving rise to the net magnetization. This

scenario of automatic allineation of magnetic moments is due to the minimisation of quantum exchange energy when magnetic moments gets alligned in one direction as in Stoner's theory came in 1933. Even in the absence of any external applied magnetic field, the material undergoes transition from the paramagnetic phase to a ferromagnetic phase with the variation of temperature from high to low. This critical temperature T_c is known as the curie temperature. In paramagnetic phase the susceptibility of material χ follows the curie weiss law as follows;

$$\chi = \frac{C}{T - T_C} \tag{1.2.1}$$

Curie weiss law fails in the environs of curie point. If the paramagnetic phase of the material transits to an antiferromagnetic phase, then the associated temperature is known as the Neël temperature T_N. Under the normal conditions, ferromagnetic materials do not exhibit the net magnetization owing to magnetization in domains oriented randomly in different directions. When an external magnetic field (H) is applied to such materials, the domains reallineates themselves to give net magnetization (M). Under the increasing magnetic field, the net magnetization increases from zero to a saturation value of M_S. However, when this external field is removed, the magnetization curve does not retraces itself under the effect of non reversibility of the domain wall displacements. So, there is a remnant magnetization M_r when the applied magnetic field goes to zero. The reverse field is applied to remove this remnant magnetization (M_r), known as the coercive field (H_C). The hysteresis curve (M-H) for ferromagnetic materials is shown below in fig. 1.2.

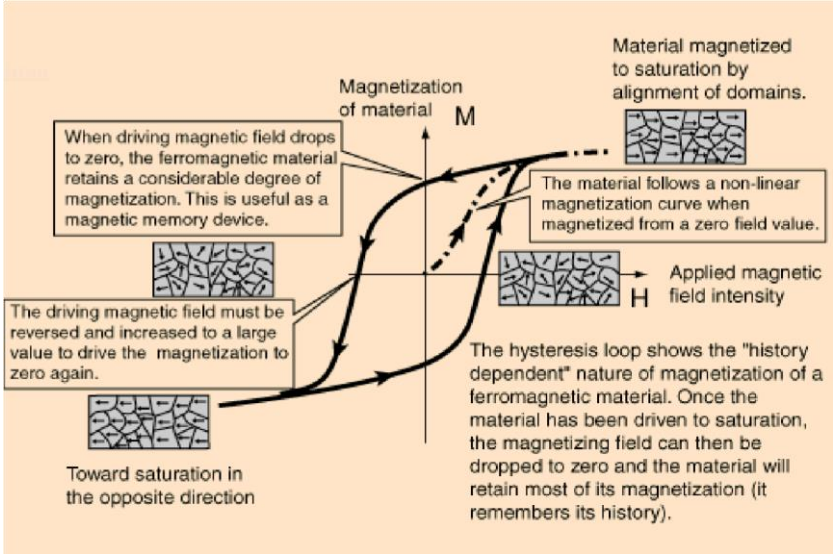

Fig. 1.2: Hysteresis curve in ferromagnetic materials

1.2.2 Ferroelectricity

It is the property by virtue of which stable spontaneous polarization can be varied hysterically by an applied electric field. Ferroelectric materials possess two or more similar crystallographic states differing each other by direction of electrical polarization. Interchange between these can be attained by an application of electric field (E) above the coercive field E_C as shown below in fig .1.3.

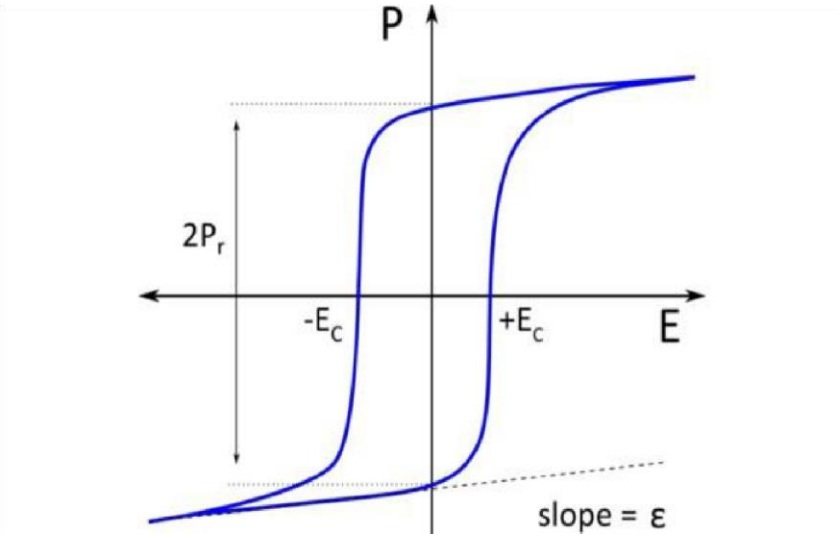

Fig. 1.3: Hysteresis curve in ferroelectric materials

When the external field is removed, a stable remnant polarization P_r is achieved in a different crystallographic direction. One of the prominent feature of ferroelectric materials is that they exhibits polarization-electric (P-E) hysteresis loop as shown below in the Fig. 1.3. Examples of ferroelectric materials are $BaTiO_3$, $PbZrO_3$, $PbTiO_3$ etc. Coercive fields and ferroelectric polarization can be calculated by the careful use of P-E loops [2, 3].

1.2.3 Ferroelasticity

It is the property of ferroic materials by virtue of which they show a spontaneous stable deformation that can be reverted by an applied stress. These materials do not follow Hooke's law and exhibit a stress – strain hysterically curve as shown in fig 1.4.

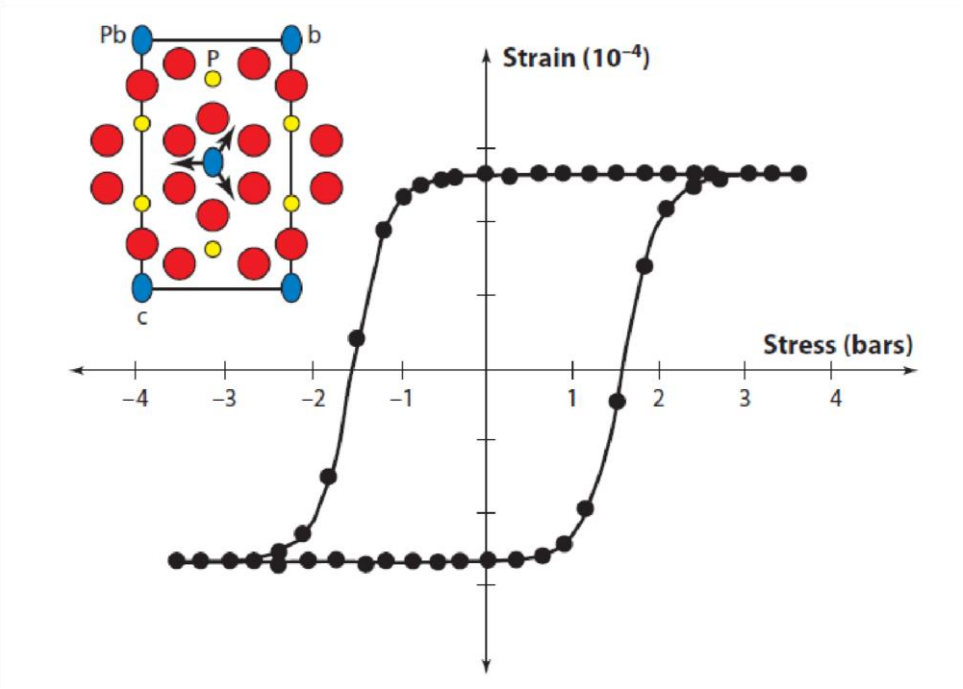

Fig. 1.4: Ferroelastic hysteresis in $Pb_3(PO_4)_2$

1.3 Magnetoelectric Coupling

Expansion of free energy term in Landau's theory demonstrates the magnetoelectric coupling in a single phase material given as follows;

$$F(E,H) = F_0 - P_i^S E_i - M_i^S H_i - \frac{1}{2}\in_0\in_{ij} E_{ij} - \frac{1}{2}\mu_0\mu_{ij}H_iH_j - \alpha_{ij}E_iH_j - \frac{\beta_{ijk}}{2}E_iH_jH_k - \frac{\gamma_{ijk}}{2}H_iE_jE_k - \ldots \tag{1.3.1}$$

where,

a) E and H are electric and magnetic fields respectively.

b) ϵ and μ are dielectric permittivity and magnetic permeability.

c) Second and third terms in the above expansion denotes the temperature dependent electrical polarization P_i^S and magnetization.

d) Fourth and fifth terms denotes the effect on electrical and magnetic behaviour due to electric and magnetic fields.

e) α_{ij} in the sixth term denotes the magnetoelectric coupling.

f) Seventh and eighth terms denotes the higher order terms.

Polarization and magnetization are obtained easily on differentiating the free energy expansion in (1.3.1) as follows;

$$P_i = -\frac{\partial F(E,H)}{\partial E_i} = P_i^S + \epsilon_0 \epsilon_{ij} E_j + \alpha_{ij} H_j + \frac{\beta_{ijk}}{2} H_j H_k + \ldots \quad (1.3.2)$$

$$M_i = -\frac{\partial F(E,H)}{\partial H_i} = M_i^S + \mu_0 \mu_{ij} H_j + \alpha_{ij} E_i + \frac{\beta_{ijk}}{2} E_i H_j + \ldots \quad (1.3.3)$$

Owing to linear magnetoelectric effect in most of the compunds, knowledge of the linear magnetoelectric coeficient (α_{ij}) tells us the dependence of polarization on magnetic and magnetization on electric field.

1.4 Types of multiferroic Materials

Multiferroic materials are divided into two classes of materials: Type 1 multiferroics and Type 2 multiferroics on the basis of nature of occurence of ferroelectricity in them [4].

1.4.1 Type 1 multiferroic Materials

These are the class of multiferroic materials in which the occurrence of ferroelectricity and ferromagnetism are due to different cations at different cationic sites (cation at A site and B site respectively) in the perovskite structure. They are marked with ferroelectricity occuring at higher temperatures than ferromagnetism. Ex. Bismuth ferrite having a spontaneous polarization of the order of 90μC/cm^2, $T_C = 1110$K and $N = 643$K, $YMnO_3$ having P ~ 6μC/cm^2, $T_C = 914$K and $T_N = 76$K, respectively [5, 6]. Type 1 multiferroic materials are further divided into subclasses based on how the ferroelectricity is originated.

a) Ferroelectricity caused due to the shifting of B ions

There are large number of perovskite materials which show ferroelectricity due to noncentro-symmetric B site cations [7]. However, in general the B site cations are responsible for the magnetic ordering in perovskite materials [8]. The solution to this problem is explained by the existence of mixed perovskites as shown in fig. 1.5 below. This figure shows the mixed perovskite with B^0 ions (green circles) causing ferroelectricity due to their shifting from the oxygen octahedra shown by the green arrows existing simultaneously with magnetism causing B^1 ions shown in red.

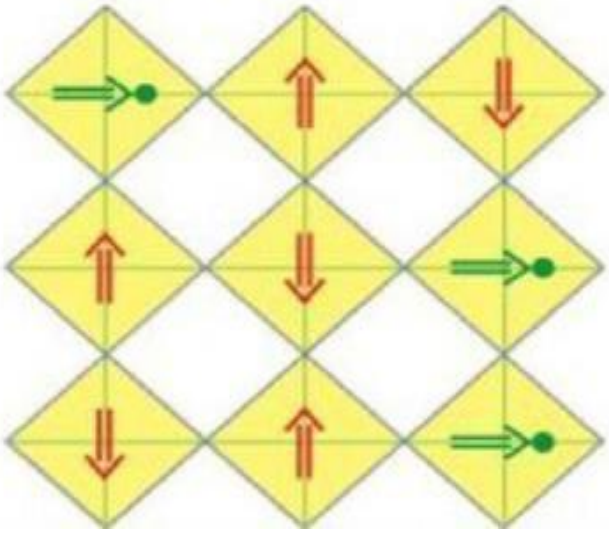

Fig. 1.5: Mixed perovskites

b) Ferroelectricity caused due to the lone pairs

Ferroelectricity in such perovskite materials is caused due to the existence of lone pairs at the A site cation in the perovskital structure as shown below in fig. 1.6.

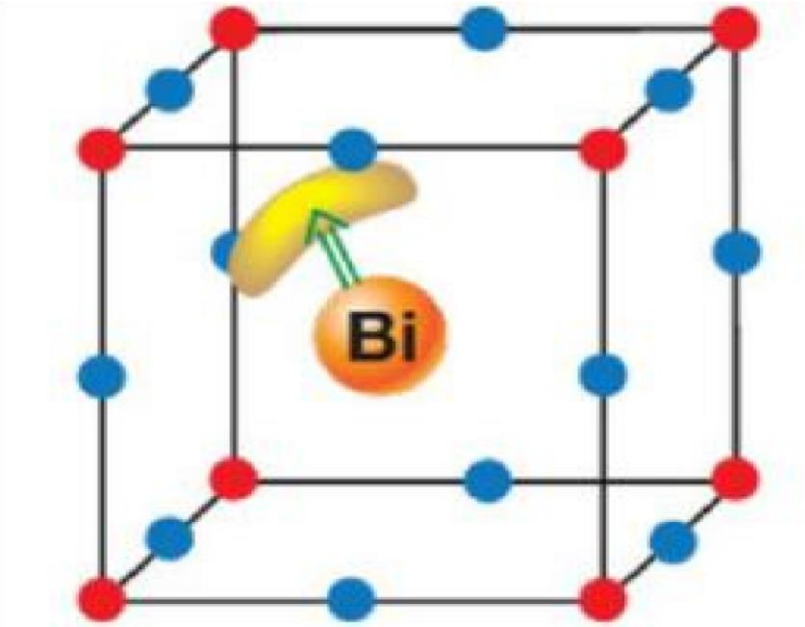

Fig.1.6: Ferroelectricity caused due to the lone pairs at Bismuth atom in the $BiFeO_3$ unit cell

Fig. 1.6 shows the Bi^{3+} ion having two outer 6s electrons not participating in any chemical bond. These two electrons are also called the lone pairs, which form a lobe as shown in yellow color in the above fig 1.6. Polarization is caused by the ordering of this lone pair electrons lobe shown by the green arrow in the above figure. While the magnetism is caused by the B site cations Ex. $BiFeO_3$, $BiMnO_3$ etc.

c) Ferroelectricity caused due to the ordering of charge

In this class of multiferroic materials, the ferroelectricity is caused by the noncentrosymmetry of charges. This non Centro-symmetry of charges is normally shown by the transition metal compounds as shown below in Fig-1.7 for magnetite (Fe_3O_4). Other examples includes $Pr_{0.5}Ca_{0.5}MnO_3$ or in Nickelates $RNiO_3$ [9, 10].

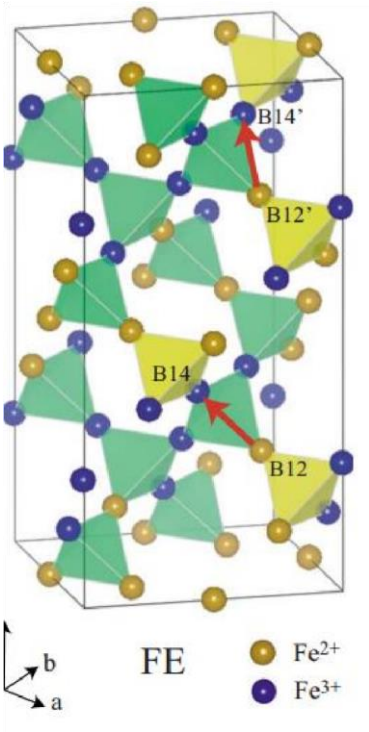

Fig.1.7: Electric dipole moments in Fe_3O_4 caused by charge shifts indicated by the red arrows

d) Ferroelectricity caused due to the geometrical factor

In this class of multiferroic materials, the ferroelectricity is caused owing to some geometric disorders in the lattice of the material. For example in $YMnO_3$, ferroelectricity is caused due to the tilting of MnO_5 octahedra with respect to the Y ions [11] as shown below in fig 1.8. As a result of

this tilting, the oxygen atoms gets closer to the Y ions in order to provide the close packing forming the dipoles shown with green colored arrows in fig 1.8. There are two down dipoles per one up dipole causing ferroelectricity in $YMnO_3$.

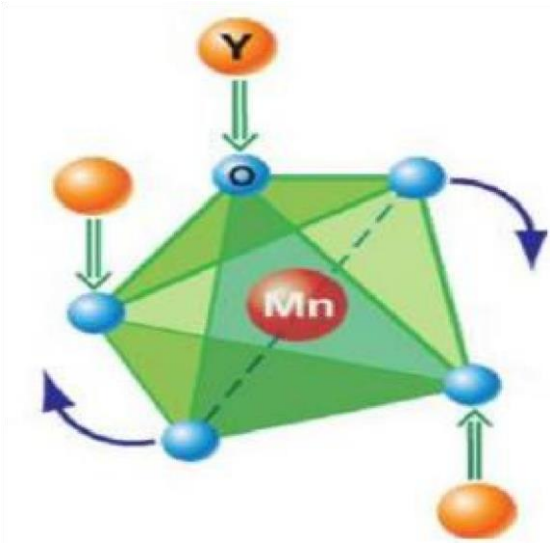

Fig.1.8: Tilting of MnO_5 octahedra with respect to Y ions shown in orange color

1.4.2 Type-2 multiferroic materials

Discovered recently, these are the class of multiferroic materials that exhibits ferroelectricity originating from the magnetism by implying strong magneto electric coupling. However, the value of polarization observed is quite small i.e. 10^{-2} μC/cm^2. Examples of this class of multiferroics are $TbMnO_3$ and $TbMn_2O_5$ [12, 13]. Type 2 multiferroic materials can be further subdivided into two class as follows;

a) Type-2 Spiral type Multiferroic materials

Found usually in frustrated magnetic systems, ferroelectricity in such materials exists in concurrence with the cycloidal magnetic phase. Examples of such materials are $TbMnO_3$, $Ni_3V_2O_6$ and $MnWO_4$. Now, for this class of multiferroic three different types of spin orderings are possible;

1. In this arrangement of spin structure, spin points along one direction but its magnitude varies as shown below in fig 1.9 below. This spin ordering does not leads to the ferroelectricity.

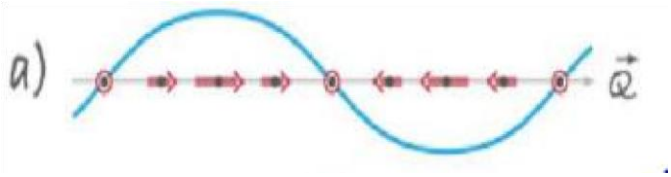

Fig. 1.9: Spin points along single direction but vary in magnitude in type-2 Spiral type multiferroic materials

2. The spin structure is in the form of cycloid with wave vector pointing along the x-axis and the spins rotating in the x-z plane as shown below in fig 1.10. This spin structure give rise to the required polarization in this class of multiferroic material.

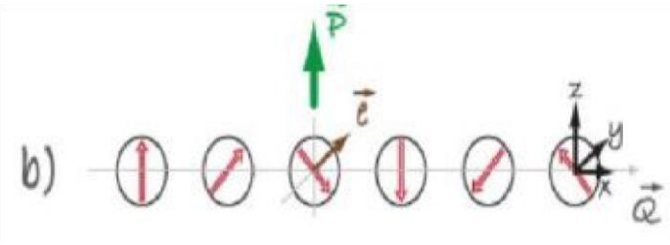

Fig. 1.10: Spins rotating in the x-z plane with wave vector pointing along the x axis in type-2 Spiral type multiferroic materials

3. In this spin structure, the wave vector Q points along the x-axis and the spins rotates in the plane peripendicular to Q as shown below in fig 1.11. This type of spin structure also does not leads to ferroelectricity.

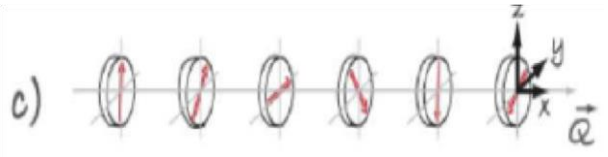

Fig. 1.11: Spins rotating in the plane peripendicular to Q pointing along the x axis in type-2 Spiral type Multiferroic materials

b) Type-2 multiferroic materials possesing collinear magnetic structures

Ferroelectricity in this class of multiferroic materials occurs in which the magnetic moments are allineated along the particular axis without necessary involvement of spin orbit interaction due to exchange restriction owing to the fact that the magnetic coupling changes with the atomic positions. Example of such a multiferroic is Ca_3CoMnO_6 [14].

1.5 Bismuth Ferrite and its properties

Bismuth ferrite is the most studied multiferroic since the advent of some really new exciting properties in Bismuth ferrite. The renaissance began in 90's with the pioneering research works of

Nicola spaldin. It has high value of $T_C = 1110\text{K}$ causing high polarization and an antiferromagnetic Neël point $T_N \sim 643\text{K}$. It can be synthesized both in the bulk and thin film forms. Bulk shows the G-type anti-ferromagnetism superposed by the long range spiral order of the magnetic spins having the length of about 62 nm whereas its thin film shows a weak ferromagnetism of about $\sim 1\mu_B$ owing to suppression of this spiral spin structure [15]. However, there is a lot of debate on the cause of weak ferromagnetism in thin films of Bismuth ferrite. It is potentially a very good compound for photovoltaic applications, spintronics etc. and lot of research is being done on it to explore new applications based on Bismuth ferrite making it one of the most interesting and demanding multiferroic material nowadays.

1.5.1 Crystal structure

Michel et al. in 1969 [16] explored the crystal structure of $BiFeO_3$ for the first time. $BiFeO_3$ in its ground state possesses the R3c point space group in a highly distorted perovskite lying in the distorted symmetry incorporating two formula units of $BiFeO_3$ [17] as shown below in fig 1.12.

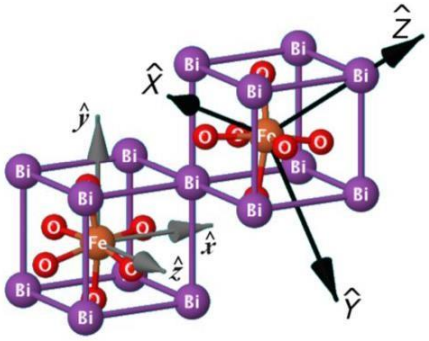

Fig. 1.12: Highly distorted rhombohedral unit cell of Bismuth ferrite made from two cubic unit cells

Bismuth ferrite in its ground rhombohedral (R3c) phase was found to have the lattice parameters $a_r = 3.965\text{Å}$ and $a_r = 89.4\text{Å}$ at room temperature [18]. Bismuth ferrite's crystal structure can also be visualized in a hexagonal cell consisting of two connected perovskite unit cubic cells aligned along their body diagonals i.e $[001]_{\text{hexagonal}}$ as shown in fig 1.13.

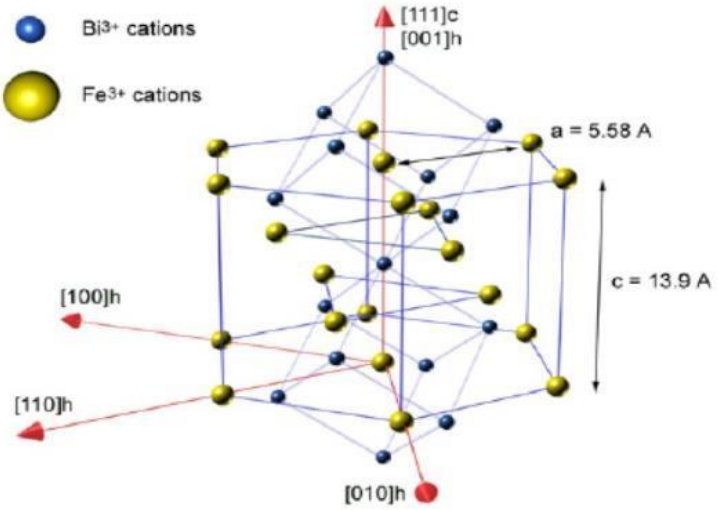

Fig.1.13: Hexagonal unit cell of $BiFeO_3$

Lattice parameter of the hexagonal frame unit cell of Bismuth ferrite are $a_{hex} = 5.58Å$ and $c_{hex} = 13.90Å$. Magnetic and electrical properties of Bismuth ferrite uses hexagonal frame unit cell for their explanation. Since, magnetic setup has been focused in this thesis for calculations. Therefore, hexagonal frame lattice parameters have been used as shown in tables (6.1) and (6.2), respectively.

1.5.2 Electrical properties

Ferroelectric ordering or spontaneous polarization P_s along $[001]_{hex}$ direction is adopted by Bismuth ferrite at a temperature T_c of 1110K [19]. Distortions of Bi^{3+} and Fe^{3+} cations from their centro-symmetric positions are responsible for the spontaneous polarization in Bismuth ferrite. A remnant polarization of more than $50\mu C/cm^2$ has been observed in single crystal and thin films of Bismuth ferrite at room temperatures [20, 21].

1.5.3 Magnetic properties

Bulk Bismuth ferrite possess a G type anti-ferromagnetic configuration caused by the transition metal cation Fe^{3+} where each Fe^{3+} cation is surrounded by six antiparallel nearest Fe^{3+} cations [22]. Antiferromagnetism is allineated along the $[001]_{hex}$ as shown in fig 1.13 shown above. In addition to G type anti-ferromagnetism, there is a superposition of a long range cycloid of the spins of Fe^{3+} cations having the reported length of ~ 620 Å [23, 24] as shown below in fig 1.14.

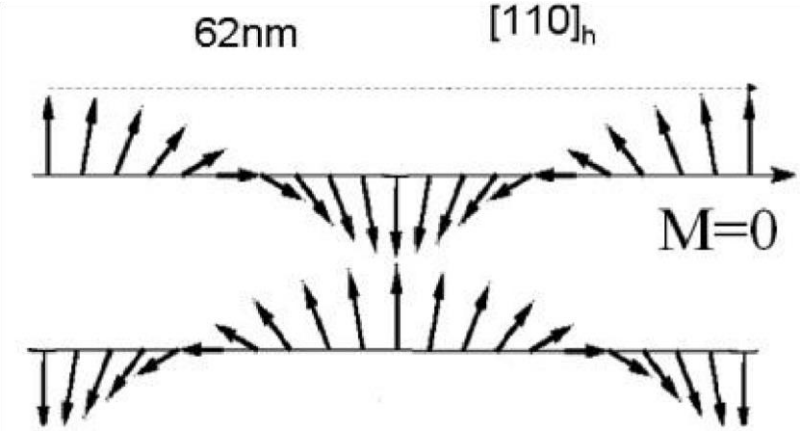

Fig. 1.14: Long range spin cycloid of Fe^{3+} cation

The cycloidal spin structure is present in the $[110]_{hex}$ direction as shown in fig 1.14.

1.5.4 Electronic properties

Theoretically, the electronic properties of $BiFeO_3$ are obtained mainly by the electronic band structure diagrams and the density of states plots in the two spin directions. In case of ground state (R3c) $BiFeO_3$ owing to the antiferromagnetic nature, the energy band structure diagrams must be equal in the two spin directions. Also, the density of states plots for O (Oxygen) and Bi (Bismuth) must be identical in the two spin directions. However, the density of states plot for Iron (Fe) must be different in the two spin directions, thereby indicating the antiferromagnetic behavior [25, 26]. In case of bulk samples of $BiFeO_3$ a direct band gap has been reported theoretically [27]. Also, a magnetic moment of ~ 3.75 μ_B [28] was observed experimentally for iron atom in $BiFeO_3$. Along with this, the theoretical works indicated a direct optical band gap in the range of around 2.5 eV [27] which lies in the visible region of the electromagnetic spectrum thereby making it a highly suitable material for photovoltaic applications [29, 30, 31].

Chapter-2

Paradigms of Density Functional Theory (DFT)

Paradigms of density functional theory

2.1 Introduction

Before discussing the paradigms of density functional theory (DFT), it would be fruitful to highlight various terminologies used within the DFT frame utilized in this thesis. Also, the property of ground state Bismuth ferrite ($BiFeO_3$) in rhombohedral (R3c) phase has been studied using DFT. It is a strongly correlated material. These strongly correlated materials are the class of materials that possess 3*d* or 4*d* electrons of the transition metals and the 4*f* or 5*f* electrons of the lanthanides and actinides which are strongly correlated. LDA (local density approximation) & GGA (generalized gradient approximation) are usually insufficient to include the strong correlations within the DFT frame. So, in order to include the strong correlations within the DFT calculations orbital dependent potentials are employed to include the effect of these *d* and *f* electrons. LDA (GGA) + U methodology is generally employed which includes the screened coulomb parameter (U) and Hund's exchange parameter (J) to incorporate the strong correlation effects of these d and f electrons. In $BiFeO_3$, 3*d* electrons are strongly correlated in Fe (transition metal) atom, thereby making it a strongly correlated system. So, this chapter will start discussing the basic paradigms of DFT and it will be extended to LDA (GGA) + U to fully understand the physics behind using it for $BiFeO_3$.

2.2 Density functional theory (DFT)

Density functional theory is the most widely used computational tool in theoretical condensed matter physics to study the condensed matter systems. The essence of DFT is to relate a many bodies interacting system through its particle density instead of its many bodies wave function. This concept pillars on the fact according to which all the properties of a system can be accurately approximated to be functions of its ground state energy. This is the well-known theorem of Hohenberg-Kohn (HK) [32]. Along with Born-Oppenheimer [33] approximation and the KohnSham (KS) equations [34], accurate DFT computations have been performed through approximate exchange – correlation (XC) potential that incorporates the results of Pauli's exclusion principle and the coulomb potential. Due to the unknown nature of the exact XC potential an intelligent approximation called LDA is used. DFT computations have satisfactorily matched the experimental data and have become a benchmark to mimic the realistic materials.

2.2.1 The concept of many bodies systems and the Born Oppenheimer approximation

The Hamiltonian for a many bodies solid state material comprising of nuclei and electrons as follows;

$$\boldsymbol{H} = -\sum_{I}\frac{\hbar^2}{2M_I}\nabla^2_{R_I} - \sum_{i}\frac{\hbar^2}{2m_e}\nabla^2_{r_I} + \frac{1}{2}\sum_{\substack{I\neq J\\ I,J}}\frac{Z_I Z_J e^2}{|R_I - R_J|} + \frac{1}{2}\sum_{\substack{i\neq j\\ i,j}}\frac{e^2}{|r_i - r_j|} - \frac{1}{2}\sum_{I,i}\frac{Z_I e^2}{|R_I - r_i|} \qquad (2.2.1)$$

where,

a) Indexes I and J are for the nuclei.
b) Indexes i and j are for the electron.
c) R_I and M_I are the positions and the masses of the nuclei.
d) r_i and m_e are the positions & the masses of electrons.
e) Z_I signifies the atomic mass of the atom I.

The first term in the above Hamiltonian denotes the kinetic energy of the nuclei. The second term denotes the kinetic energy of the electrons. The third term denotes the nucleus-nucleus interaction energy (columbic). The fourth term signifies the electron-electron columbic interaction energy and the last term is the potential energy term of the columbic nucleus-electron interactions. The corresponding time independent Schrödinger wave equation can be written as;

$$\boldsymbol{H}\,\Psi[(R_I),(r_i)] = E\,\Psi\,[(R_I),(r_i)] \qquad (2.2.2)$$

Here, $\Psi\,[(R_I),(r_i)]$ denotes the total wave function of the solid state system. So, solving this Schrödinger wave equation gives all the information about the solid state system. But the problem is that it cannot be solved due to its huge size. The solution to this problem lies in Born Oppenheimer approximation coined in 1927 [33]. It assumes that the nuclei being much heavier than the electrons and have fixed positions with electrons hovering around them. This assumption revolutionarily separated the total wave function into two parts as follows

$$\Psi[(R_I),(r_i)] = A[(R_I)]\,B[(r_i),(R_I)] \qquad (2.2.3)$$

Where, $A[(R_I)]$ describes the nuclei and $B[(r_i), (R_I)]$ describes the electrons with respect to the position of the nuclei. By the application of this approximation the equation (2.2.2) can be broken into two separate Schrödinger wave equations;

$$\boldsymbol{H}_{\text{electron}}\, B\,[(r_i), (R_I)] = V\,(R_I) B[(r_i), (R_I)] \tag{2.2.4}$$

where,

$$\boldsymbol{H}_{\text{electron}} = -\sum_i \frac{\hbar^2}{2m_e}\nabla_{r_i}^2 + \frac{1}{2}\sum_{\substack{I\neq J\\ I,J}} \frac{Z_I Z_J e^2}{|R_I - R_J|} + \frac{1}{2}\sum_{\substack{i\neq j\\ i,j}} \frac{e^2}{|r_i - r_j|} - \frac{1}{2}\sum_{I,i} \frac{Z_I e^2}{|R_I - r_i|} \tag{2.2.5}$$

Which determines the eigenvalues of the energy $V\,[(R_I)]$ depending on the positions of the nuclei.

and

$$\left[-\sum_I \frac{\hbar^2}{2M_I}\nabla_{R_I}^2 + V(R_I)\right] A[(R_I)] = EA[(R_I)] \tag{2.2.6}$$

Once $V\,[(R_I)]$ is obtained from the equation (2.2.4) it is fed into equation (2.2.6) to determine the motion of the nuclei. With these two steps the whole problem gets solved. However, still after the application of Born Oppenheimer approximation the problem remained mighty owing to the large size of Hamiltonians.

2.2.2 The Theorems of Hohenberg and Kohn

In 1964, Hohenberg and Kohn [32] proved that the density functional theory satisfactorily applies not only to solid state systems having electrons with fixed nuclei but also to systems having interacting particles in an external potential $V_{ext}(r)$. This theory rests on two basic theorems. a) Theorem 1

The external potential $V_{ext}(r)$ of a solid state system comprising of interacting particles is uniquely determined by its ground state particle density $n(r)$, subjected to an external potential $V_{ext}(r)$. In other words, the full Hamiltonian or all the ground and the excited states can be extracted from the ground state particle density of a solid state system.

$$[n(r)] \rightarrow [V_{ext}(r)] \tag{2.2.7}$$

However, there is no exact numerical recipe to get this transformation.

b) Theorem 2

This theorem states the existence of universal functional of energy F (n(r)) depending solely on the density n(r), valid for any external potential $V_{ext}(r)$. For a given value of $V_{ext}(r)$, the exact ground state energy of the solid state system is obtained from the global minimum of the following functional;

$$E[n(r)] = [n(r)] + \int n(r)V_{ext}(r)dr \qquad (2.2.8)$$

Thus, this theorem states the existence of exact ground state energy and density as determined from the minimization of the energy functional (n(r)).

These theorems can be extended to spin density functional theory [35]. This theory suggests two different types of densities, namely the particle density ($n(r) = n_{up}(r) + n_{down}(r)$) and the spin density ($s(r) = n_{up}(r) - n_{down}(r)$), up and down signifies two different kinds of spins. The corresponding energy functional is E[n(r), s(r)]. Since, Bismuth ferrite ($BiFeO_3$) is a magnetic system having net spins on the Fe atoms, spin density functional theory has been used to investigate the ground state properties of ($BiFeO_3$) in this thesis.

2.2.3 The Kohn-Sham equations

Hohenberg and Kohn theorems were put to practical use by Kohn Sham equations [34]. The formalism proposed by Kohn was so powerful that Kohn was honored noble prize in chemistry in 1998. In KS formalism, the many bodies solid state system is replaced by an ancillary independent particle system while assuming the same ground state density for both the systems. This ancillary system comprises of the electrons moving within an effective Kohn-Sham single particle potential $V_{k-s}(r)$ the Hamiltonian for this ancillary system is written as;

$$\boldsymbol{H}_{k-s} = -\frac{1}{2}\nabla^2 + V_{k-s}(r) \qquad (2.2.9)$$

[Here the units taken are $\div$ $\hbar = m_e = e = 4\pi/\varepsilon_0 = 1$]

Now, for the system comprising of N electrons (independent), the ground state can be extracted by solving N-one electron Schrödinger wave equations;

$$\left(\frac{1}{2}\nabla^2 + V_{k-s}(r)\right)\Psi_i(r) = E_i\Psi_i(r) \quad (2.2.10)$$

Where, N and $\Psi_i(r)$ are orbitals each consisting of one electron having the lowest Eigen values E_i. Now, the density of this ancillary system is extracted using the following;

$$n(r) = \sum_{i=1}^{n}|\Psi_i(r)|^2 \quad (2.2.11)$$

Which obeys the condition of conservation i.e.

$$\int n(r)dr = N \quad (2.2.12)$$

So, the universal functional F [n(r)] for the ancillary system can be written as

$$F[n(r)] = T[n(r)] + E_{Hartree}[n(r)] + E_{XC}[n(r)] \quad (2.2.13)$$

where, T [n(r)] is the kinetic energy term of the non-interacting independent particle solid state systems. $E_{Hartree}[n(r)]$ is the energy due to electrostatic interaction of electrons.

$$E_{Hartree}\ [n(r)] = \iint \frac{n(r)n(r1)}{|r-r'|}drdr' \quad (2.2.14)$$

E_{xc} [n(r)] is the XC energy, which is the difference between exact and non-interacting kinetic energies along with the non-classical contribution of the electronic interactions. Minimization of the energy functional, $E[n(r)] = [n(r)] + \int n(r)V_{ext}(r)dr$ subject to the conservation of N electrons gives the ground state energy of the multi-electron solid state system.

So, $$[F(n(r)) + \int n(r)V_{ext}(r)dr - \mu(\int n(r)dr - n] = 0 \quad (2.2.15)$$

gives $$\mu = \frac{\delta F(n(r))}{\delta n(r)} + V_{ext}(r) = \frac{\delta F(n(r))}{\delta\, n(r)} - V_{ext}(r) \quad (2.2.16)$$

Where μ is the chemical potential.

Hence,

$$V_{ks}(r) = V_{ext}(r) + V_H(R) + V_{XC}(r) = V_{ext}(r) + \frac{\delta E_H(N(R))}{\delta N(R)} - \frac{\delta E_{XC}(N(r))}{\delta n(r)} \quad (2.2.17)$$

Here, $V_{ks}(r)$ is the one particle potential of the ancillary multi-electron independent particle system. Equations (2.2.10), (2.2.11), (2.2.17) together constitutes the Kohn-Sham equations.

However the Kohn Sham's theory is approximate owing to unknown XC energy functional E_{XC} (n(r)) or potential $V_{xc}(r)$ restricting this theory from describing the solid state material satisfactorily. Approximations are therefore used for the XC potential. The most commonly used approximations for the XC potential are local density approximation (LDA) and generalized gradient approximation (GGA).

2.2.4 LDA and GGA -Approximations to the exchange correlation potential

So, the nature of exchange-correlation potential must be known in order to construct the Kohn-Sham potential for solving the Kohn Sham equations self-consistently. In their work where they proposed their scheme they also pointed a form of this functional commonly known as the local density approximation (LDA). In LDA at each point r the XC energy for an electron at that point r is assumed to be identical with that of homogeneous electron gas having the same density of electrons at that point r. The exchange energy functional E_{xc} (n(r)) can be written as;

$$E_{XC}^{LDA}(n(r)) = \int n(r)[\in^{homo}_{x}(n(r)) + \in^{homo}_{x}(n(r))dr \quad (2.2.18)$$

$$= E_X^{LDA}\big(n(r)\big) + E_C^{LDA}\big(n(r)\big) \quad (2.2.19)$$

In (2.2.18) it can be noted that the XC energy density is split into two exchange energy densities i.e. $\in_w^{homo}\big(n(r)\big)$, the correlation energy density and $\in_x^{homo}\big(n(r)\big)$, thereby splitting the XC energy functional into exchange and correlation energy functional under LDA as shown in equation (2.2.19). The various LDA approximations commonly used in DFT calculations are Vosko-Wilk-Nusair [36], Perdew-Zunger [37], Cole Perdew [38] and Perdew wang [39]. However the realistic solid state material may contain in homogeneity in the charge densities different from the homogenous electron gas considered. In such cases the generalized gradient approximation (GGA) incorporating corrections for gradient of densities and higher spatial derivative of the electron density gives better results. The most commonly used GGA's are the ones proposed by Becke [36], Perdew et *al.* [41] and Perdew, Booke and Enzerhof [42]. Ever after using these improved approximations (LDA and GGA), they are not able to handle the solid state materials having strongly correlated and localized electrons.

2.2.5 Processing strongly correlated electrons within the DFT frame

As discussed earlier strongly correlated materials are the ones possessing metal atoms with partially filled d and f shells. LDA and GGA cannot handle such systems accurately. In strongly

correlated systems, the electrons in d and f orbitals are localized strongly thereby deviating from the homogenous electron gas model .A strong columbic interactions are felt by these localized electrons which is not incorporated in LDA and GGA. In order to cover the effects of these strongly correlated electrons LDA + U [44] method is employed most commonly. In LDA + U method, the effect of delocalized *s* and *p* electrons are covered under DFT using LDA/GGA and the effects of localized *d* or *f* electrons are covered using the orbital dependent term $\frac{1}{2} U \sum_{i \neq j} n_i n_j$ describing the strong columbic interactions among the *d* or *f* electrons. Here n_i denotes the *d* and *f* orbital occupancies. The total energy in L(S) DA + U method [43] is given as;

$$\mathbf{E_{LSDA+U}}[\rho_\sigma(r), n(\sigma)] = E_{tot}^{LDA+U}[\rho_\sigma(r)] + E^{U}[(n(\sigma)] - E_{dc}[n(\sigma)] \qquad (2.2.20)$$

Where, σ denotes the spin index, $\rho_\sigma(r)$ is the electron density for spin-σ electrons and [n (σ)] is the Density matrix of *d* or *f* electrons for spin-σ. The first term is the standard L(S) DA functional and second is the electron-electron coulomb interaction energy.

Chapter-3

Literature Review

Literature Review

1. I. Sosnowska *et al.* in 1994 [28] investigated the crystal and the magnetic structure of the Bismuth ferrite using neutron diffraction studies. They found the refinement of crystal and magnetic structure of Bismuth ferrite at room temperature using R3c space group and the hexagonal unit cell. They reported the magnetic moment of ~3.70μ_B per Fe^{1+} ion arranged anti-Ferro magnetically in $BiFeO_3$ at 293K.

2. J.B Neaton *et al.* in 2005 [44] performed the first principle study of spontaneous polarization in multiferroic $BiFeO_3$. They studied the structural, electronic and magnetic as well as polarization in Bismuth ferrite using LSDA + U and LSDA under the DFT frame. In their structural study they found the R3c space group structure in the ground state for Bismuth ferrite. Also, they found the structural parameters in accord with reported by F. Kubel and H. Schmid [45]. In their study on electronic properties of ground state $BiFeO_3$ they obtained an energy band gap of 0.4eV from LSDA and 1.3 & 1.9 eVs respectively for U_{eff} =2eV and 4eV respectively under LSDA + U. They ignored the spin orbit interactions in their investigations. They also found a G type anti-ferromagnetic structure for ground state $BiFeO_3$ with a magnetic moment of ~3.3μ_B from LSDA and 3.8 μ_B and 4 μ_B agreeing closely with that reported by Sosnowska *et al.* [46]. Also, in their first principle study they found the large values of polarizations between 80 – 100 $\mu C/cm^2$ in agreement with highly distorted perovskite structure for rhombohedral (R3c) $BiFeO_3$.

3. P Ravindran *et al.* in 2006 [47] theoretically studied the magneto electric behavior of $BiFeO_3$. They used GGA within the DFT frame to perform their theoretical calculations. In their structural stability studies they found a pressure induced structural transition from polar R3c structure to a Pnma structure around 130 kbar. They also identified two ferroelectric phases namely tetragonal P4mm and monoclinic Cm respectively. They also found large energy differences between various types of anti-ferromagnetic configurations (A, G and C types) in $BiFeO_3$ with A and G type anti-ferromagnetic setup showing the insulating behavior for in polarization is essentially due to the displacement of Bi relative to the center of FeO_6 octahedra of $BiFeO_3$.Also they found that the bonding between the constituent atoms (Ex. Between Fe

and O) is not purely ionic, containing directional covalent character in it via charge density plot, electron localization function plot etc.

4. S. J Clark *et al.* in 2007 [48] studied the band gap and schottky barrier heights of multiferroic $BiFeO_3$. They found a band gap of 2.8eV which was much higher than found from LSDA by Neaton *et al.* [44]. They suggested that their calculated band gap and schottky barrier heights were large to indicate the small electronic leakage.

5. H. Wang *et al.* in 2009 [25] performed the first principle study on the electronic and optical properties of $BiFeO_3$. They found an indirect band gap of 1.06eV.

6. S. Ju *et al.* in 2009 [49] studied the electronic structure, linear and nonlinear optical responses in magneto electric multiferroic material $BiFeO_3$. They used GGA + U for their DFT calculations with U = 7eV and J = 0.9eV for Fe 3*d* electrons. They found that the band gap reaches up to 2.5eV when U was taken larger than 7eV. They also found a magnetic moment of 4.31 μ_B on Fe atoms in $BiFeO_3$.

7. Y. Wang *et al.* in 2011 [50] studied the lattice dynamics of $BiFeO_3$. Using density functional theory. They determined phonon dispersions, phonon density of states and the heat capacity while paying special attention to the low temperature range and found that the pure phonon model can describe the curve shape of heat capacity at low temperatures. They also proposed that no gapped magnon states exist for $BiFeO_3$ that contributes to the heat capacity of $BiFeO_3$. in the temperature range of 2-30 K. They performed the DFT calculations based on the 10 atoms unit cell of $BiFeO_3$ in which they kept the spins of the two Fe atoms opposite in order to preserve the G type spin configuration. They used GGA + U in all their calculations with the value of U – J = 6eV. They found a band gap of 2.46eV and magnetic moment value of ~4.26μ_B.

8. L. Qiang *et al.* in 2013 [26] performed the first principle calculations while employing the quasi harmonic Debye model to investigate the thermodynamic properties and the phase transition between the trigonal R3c structure and the orthorhombic Pnma structure. They found that this phase transition is a first order anti-ferromagnetic to non-magnetic and insulator to metal type transition according to equal Gibbs free energies and occur at 10.56GPa. From their

DFT calculations they found that the ground state $BiFeO_3$ is anti-ferromagnetic in nature with equal total density of states plots in the two spin directions i.e. spin up and spin down.

9. J. Kaczkowski *et al.* in 2015 [51] performed the DFT+U calculations and found the G type anti-ferromagnetism in R3c, Pnma, Pn21a phases and a C type anti-ferromagnetism in case of Cm space groups of $BiFeO_3$.In all these structures they found the band gaps of 2.26 eV (2.27 eV) for R3c, 1.91 eV (1.66 eV) for Pnma, 1.99 eV (2.18 eV) for $Pn2_1a$ and 2.09 eV (2.55 eV) for Cm respectively.

10. P. Singh *et al.* in 2015 [52] studied the effect of isovalent nonmagnetic Fe site doping on the electronic structure and spontaneous polarization of $BiFeO_3$.They used GGA in their DFT calculations and mentioned U_{eff} =4eV as the appropriate choice for determining the band gap as well as the magnetic moments on Fe atoms in $BiFeO_3$. They adopted G type antiferromagnetic ordering coupled with collinear spin structure in order to simplify the calculations. They also mentioned that the 10 atoms unit cell of $BiFeO_3$ is appropriate for performing the DFT calculations of pure ground state $BiFeO_3$.

Chapter-4

Motivation

Motivation

Bismuth ferrite is the most studied multiferroic with thousands of experimental research papers already published around the world. A lot of theoretical (First principle calculations) work has been done on bismuth ferrite in order to estimate its electronic, optical as well as magnetic properties majorly based on the XRD (X-ray diffraction) data of F. Kubel and H. Schmid [45]. R. Palai et al. [53] had experimentally found that as the temperature is increased the band gap of bismuth ferrite decreases and goes to zero indicating the metal-insulator transition. They also performed the screened exchange theoretical calculations on the cubic and orthorhombic phases of bismuth ferrite indicating the metal- insulator transition [53]. However, their theoretical study was not the total energy calculation which cannot assure the stability of phases they assumed. So, to the best of our knowledge no theoretical verification has been done till now to study the effect of calcination temperatures of the ground state pure rhombohedral (R3c) bismuth ferrite on its energy band gap in rhombohedral phase. In this thesis theoretical first principle calculation of density functional theory has been performed based on the experimentally obtained rietveld refinement data given in Table-6.1 and 6.2 for 500°C and 600°C respectively in order to theoretically study and verify the effect of calcination temperatures of ground state rhombohedral (R3c) pure bismuth ferrite on its energy band gap.

Chapter- 5

Computational approach and

The

Computational details

Computational approach and the Methodologies used for calculations

In this thesis, the theoretical calculations for the ground state rhombohedral (R3c) pure phase bismuth ferrite were performed using GGA+U [43] within the TB-LMTO-ASA code [54, 55]. Two parameters are used under the GGA+U methodology in order to treat the strongly correlated d states of Fe atoms in $BiFeO_3$, namely the Hubbard parameter (U) and the exchange interaction parameter (J) [43]. We define the effective Hubbard parameter Ueff = U - J for the sake of convenience. During the self-consistent field (SCF) calculations, the Hubbard parameter U was made a free parameter keeping the exchange parameter J constant at a value of 1eV thereby giving various values of effective Hubbard parameters U_{eff}. The value of effective Hubbard parameter U_{eff} was thus varied between 1 to 7 eV in order to get the values of the magnetic moment on the Fe atoms in $BiFeO_3$ and the values of the energy band gaps. After that the appropriate value of U_{eff} giving the value of band gap close enough to that observed from the experiments was chosen.

A 4×4×4 Monkhorst pack k point mesh [56] along with the tetrahedron method incorporating Blöchl correction [57] were used to perform the brillouin zone integrations. In the SCF calculations, collinear spin structure owing to very small value of non-collinearity in the experimental structure was used in order to simplify the calculations [52]. Also, the spin orbit interactions among the Fe atoms in $BiFeO_3$ were neglected owing to very small value of 0.06eV calculated by Dr. Yoshiro Nohara for the use in this thesis (Kindly refer to the acknowledgements). Such a small value of the spin orbit interactions does not play an important role in the SCF calculations. A unit cell containing 10 atoms of $BiFeO_3$ was used to perform the SCF calculations while keeping the spins of Fe atoms in the opposite direction to maintain the G type anti-ferromagnetic order [50]. Lastly, the SCF calculations were performed using the values of fractional coordinates of the atoms in $BiFeO_3$ at temperatures of 500^0C and 600^0C given in the tables 6.1 and 6.2 with an initial guess of magnetic moment of $5\mu_B$ on each Fe atoms.

Chapter-6

Results and Discussions

Results and Discussions

6.1 Optimization of the Hubbard parameter U_{eff}

In order to perform the SCF (Self consistent field) calculations, the TB-LMTO-ASA code version 47 [54, 55] was employed. For theoretical calculations of ground state rhombohedral (R3c) phase pure $BiFeO_3$ calcined at 500^0C, the lattice parameters and the fractional coordinates of atoms [58] were used as given below in table 6.1.

Table. 6.1: Fractional coordinates and lattice parameters of ground state pure $BiFeO_3$ calcined at 500^0C

Composition $BiFeO_3$	Atom	Fractional Co-ordinates			Lattice Constant (Å)	Band Gap (eV)
		x	y	z		
At 500 ^{0}C Space Group: R3c	Bi	0	0	0	a = 5.577, c = 13.8463	2.16
	Fe	0	0	0.2212		
	O	0.4748	0.0178	-0.0563		

Using the above mentioned data as shown in Table 6.1 and with an initial guess of magnetic moment of ~5μ_B on a high spin Fe^{3+} ion, SCF calculations were performed by varying the effective Hubbard parameter (U_{eff}) defined as $U_{eff} = U - J$ between 1 to 7 eV while keeping J=1 eV constant to get the variations in band gap and magnetic moment on Fe atom in $BiFeO_3$ as shown in Figs-6.1 and 6.2 respectively. From Fig-6.1 it was observed that U_{eff} = 5 eV (U = 6 eV and J = 1 eV) gave the close estimate of the value of band gap of ~ 2.25 eV in close agreement with that observed from the experiment i.e. 2.16 eV as given above in table-6.1 with a slightly overestimated value of magnetic moment of ~4.11 μ_B. However from Fig-6.2 it was observed that the value of U_{eff} = 0.5 eV (U = 1.5 eV and J = 1 eV) gave the magnetic moment of ~ 3.75 μ_B which exactly agrees with that reported in the experiments i.e. 3.75 μ_B [28] with an underestimated value of the band gap of ~ 0.92eV. Since our aim is to study the effect of calcination temperatures on the band gap of ground state rhombohedral (R3c) phase pure bismuth ferrite we conclude that the value of effective

Hubbard parameter U_{eff} = 5 eV (U = 6 eV and J = 1 eV) is appropriate for studying the band gap variations with temperature.

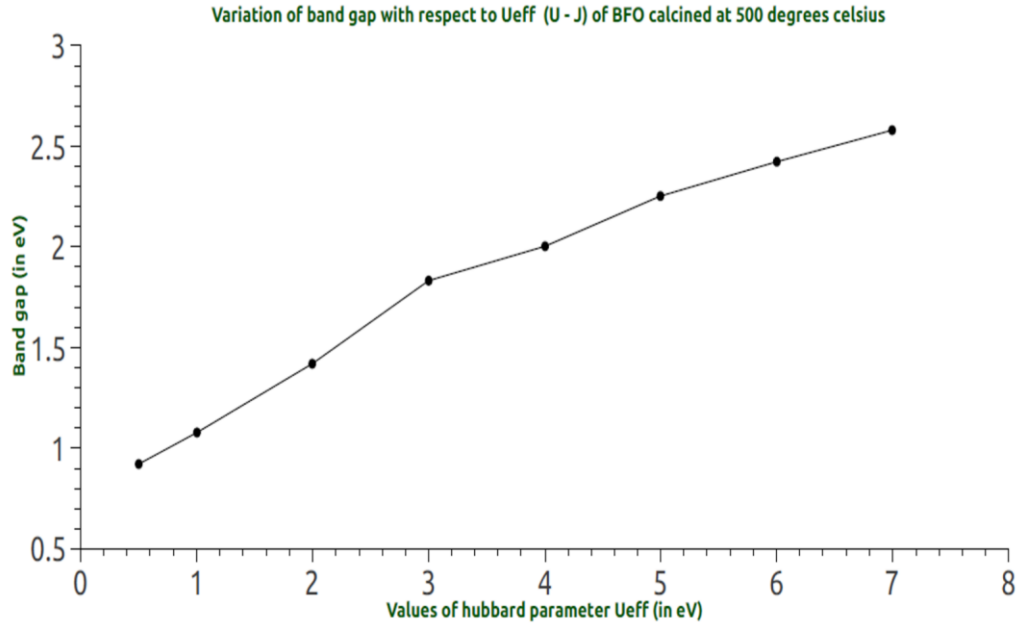

Fig. 6.1: Variation of band gap with respect to the Hubbard parameter U_{eff}

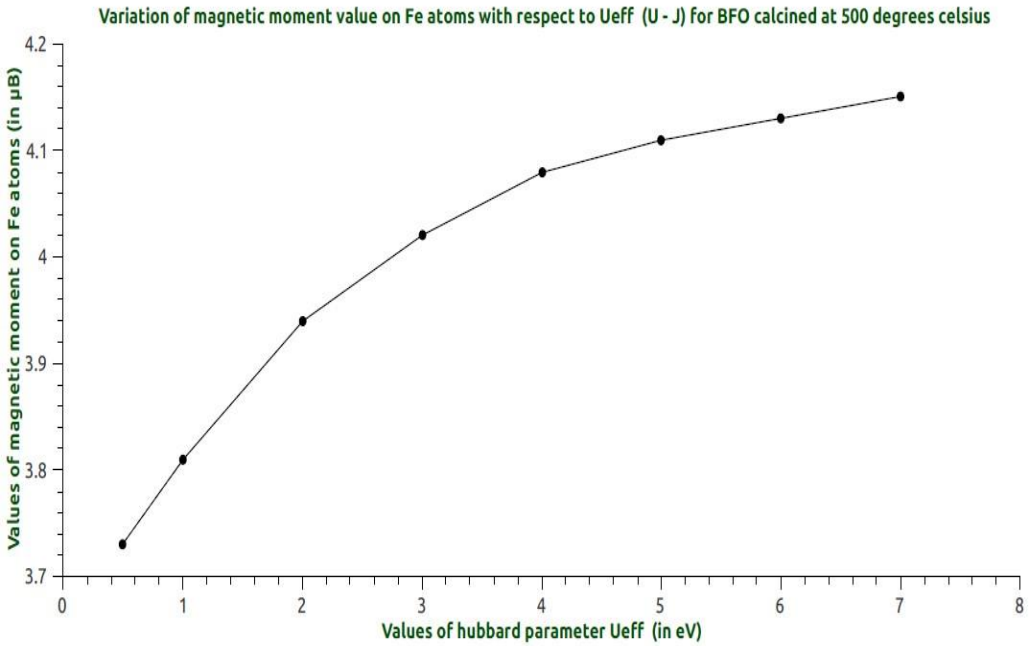

Fig. 6.2: Variation of magnetic moment on Fe atom with respect to the Hubbard parameter U_{eff}

6.2 Electronic and magnetic properties of a pure ground state $BiFeO_3$ calcined at 500°C

Using the above optimized value of Hubbard parameters U = 6 eV and J = 1 eV i.e. U_{eff} = 5 eV appropriate to study the band gap variation, the SCF calculations were performed. In order to study the nature of band gap and the type of magnetic ordering in ground state rhombohedral (R3c) phase $BiFeO_3$ calcined at 500^0C the energy band structure diagrams were obtained in the spin-1 and spin-2 direction channels as shown below in figs. 6.3 and 6.4 respectively.

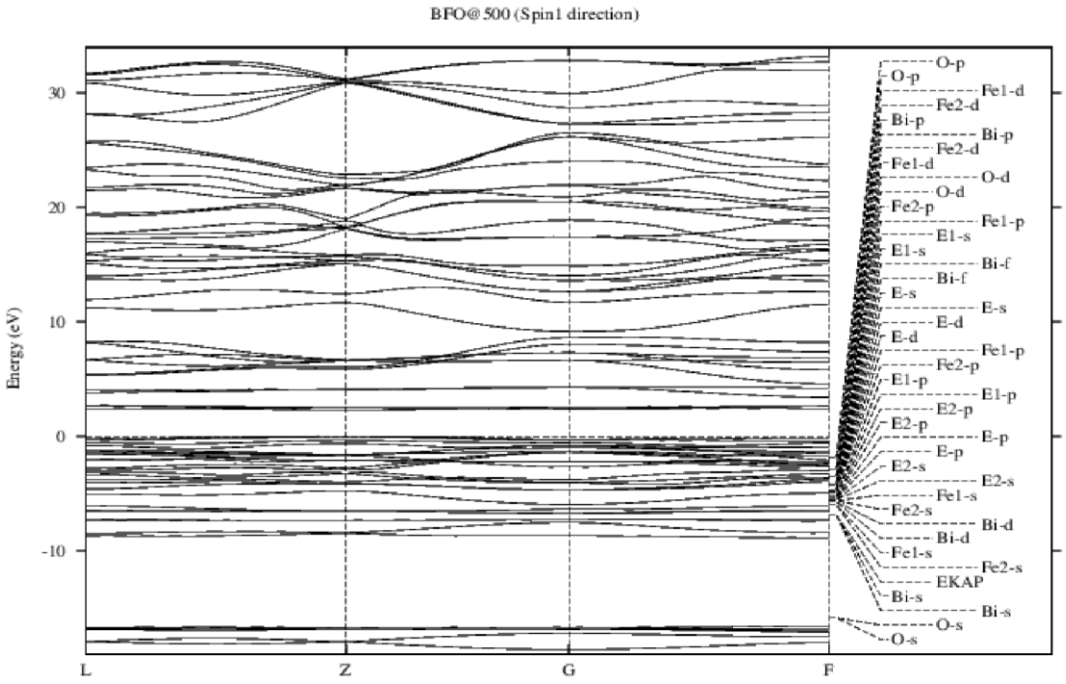

Fig. 6.3: Energy band structure diagram of ground state $BiFeO_3$ in Spin-1 direction

From figs. 6.3 and 6.4 it was observed that the ground state rhombohedral (R3c) phase $BiFeO_3$ possess a direct band gap because the maximum of valence band and the minimum of conduction band lies along the same vertical Z line which agrees with that observed experimentally [58]. Also it was observed that the band structure diagrams are identical in the two spin directions (spin-1 and spin-2) indicating the anti-ferromagnetic behavior in ground state $BiFeO_3$ [25].

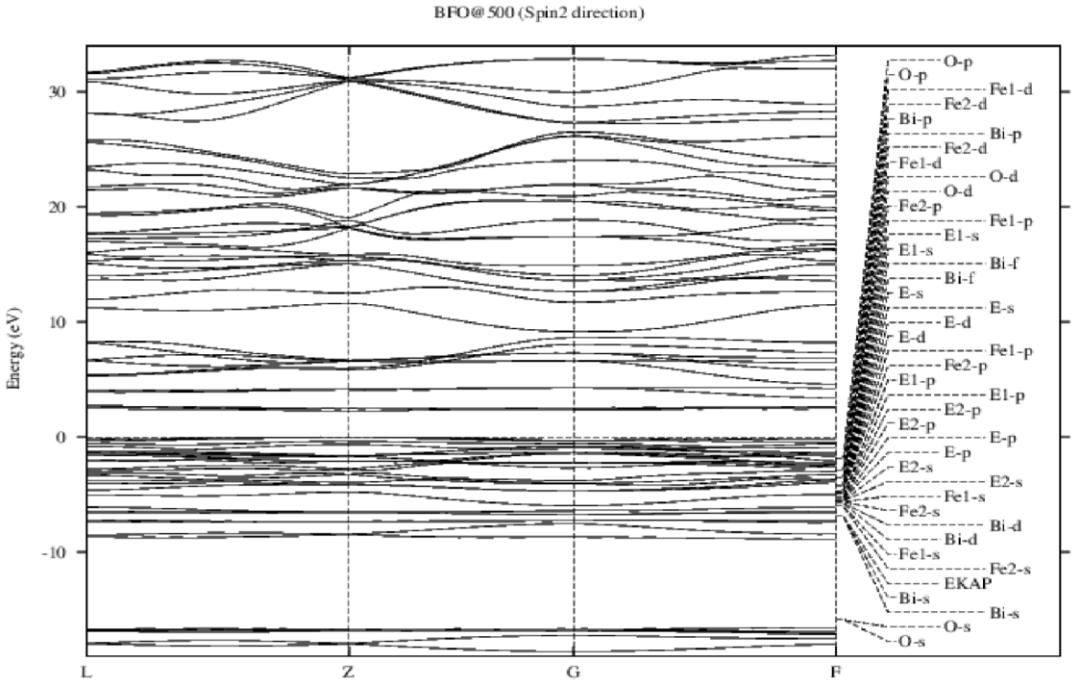

Fig. 6.4: Energy band structure diagram of ground state $BiFeO_3$ in Spin-2 direction

In order to extract the energy band gap value the total density of states plot was obtained as shown below in fig. 6.5. From the fig 6.5 an electronic band gap of 2.25 eV was observed which closely matched with that obtained from the experiments i.e. 2.16 eV as given in the Table-6.1 [58] with the value of magnetic moment on Fe atoms of ~ 4.11 μ_B. Next in order to further verify the magnetic ordering in the ground state $BiFeO_3$, the partial density of states plots for Bi (Bismuth), O (Oxygen), Fe1 (Iron) and Fe2 (Iron) in spin-1 and spin-2 directions along with total density of states plots in spin-1 and spin-2 directions were obtained as shown below in figs. 6.6, s6.7, 6.8, 6.9, 6.10, 6.11, 6.12, 6.13, 6.14 and 6.15 respectively.

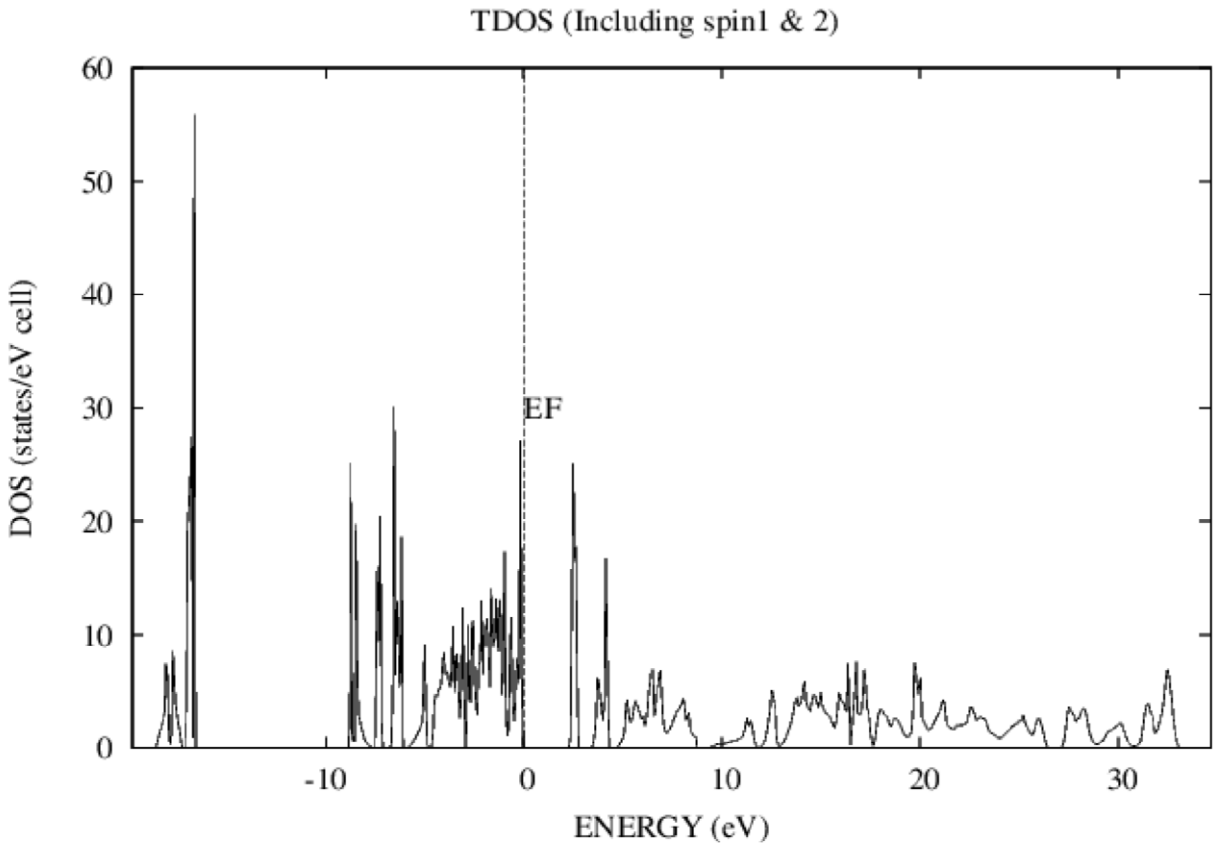

Fig. 6.5: Total density of states plot including contributions from both spin-1 and spin-2 directions

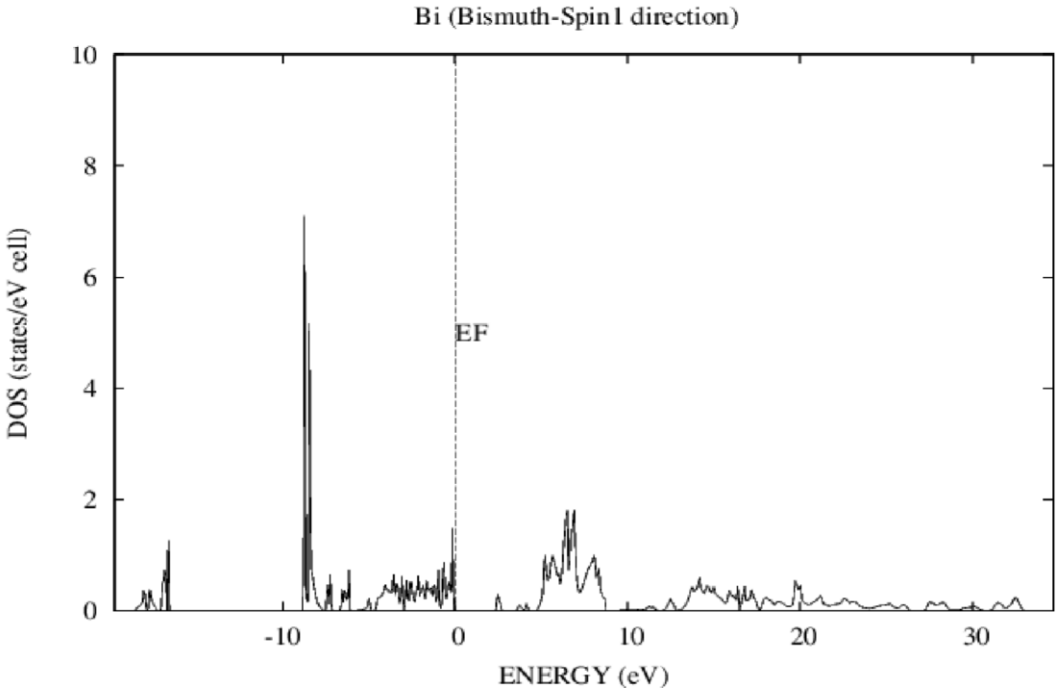

Fig. 6.6: Partial density of states plot for Bi (Bismuth) in spin-1 direction

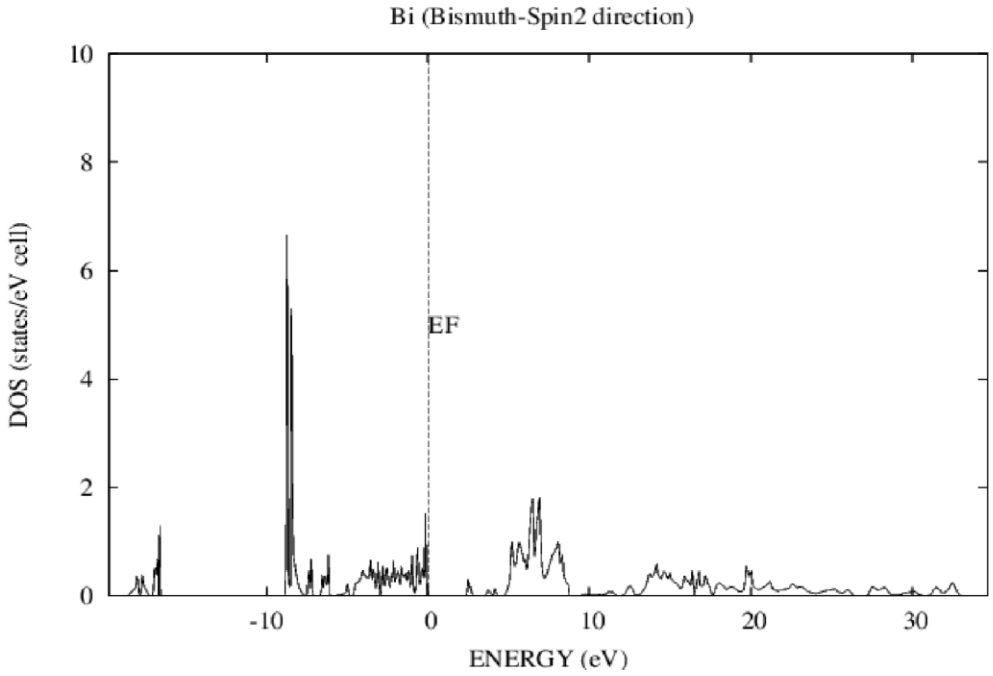

Fig. 6.7: Partial density of states plot for Bi (Bismuth) in spin-2 direction

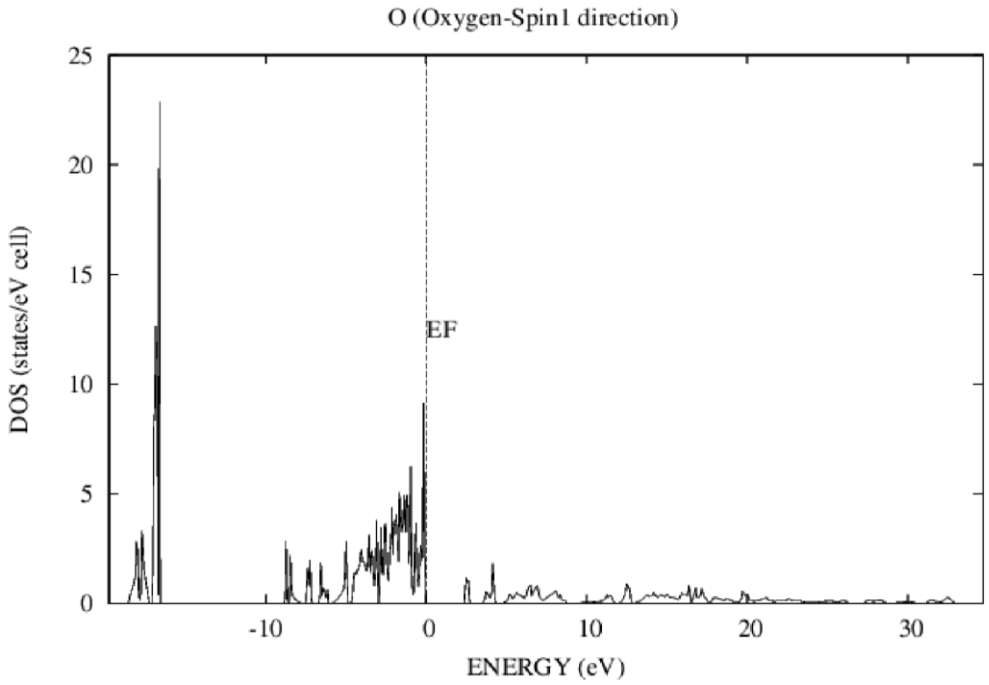

Fig. 6.8: Partial density of states plot for Oxygen in spin-1 direction

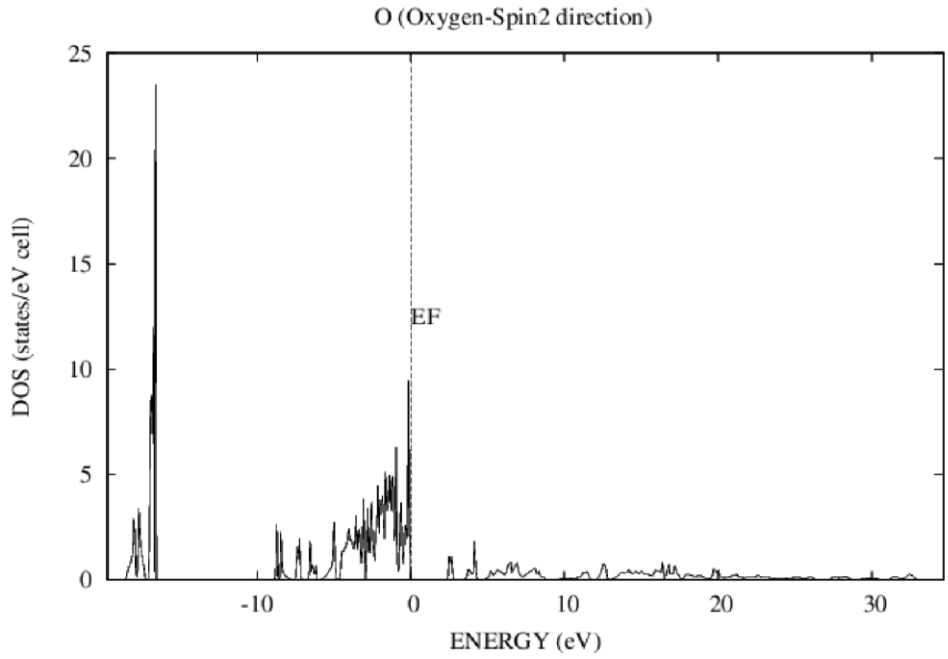

Fig. 6.9 Partial density of states plot for Oxygen in spin-2 direction

:

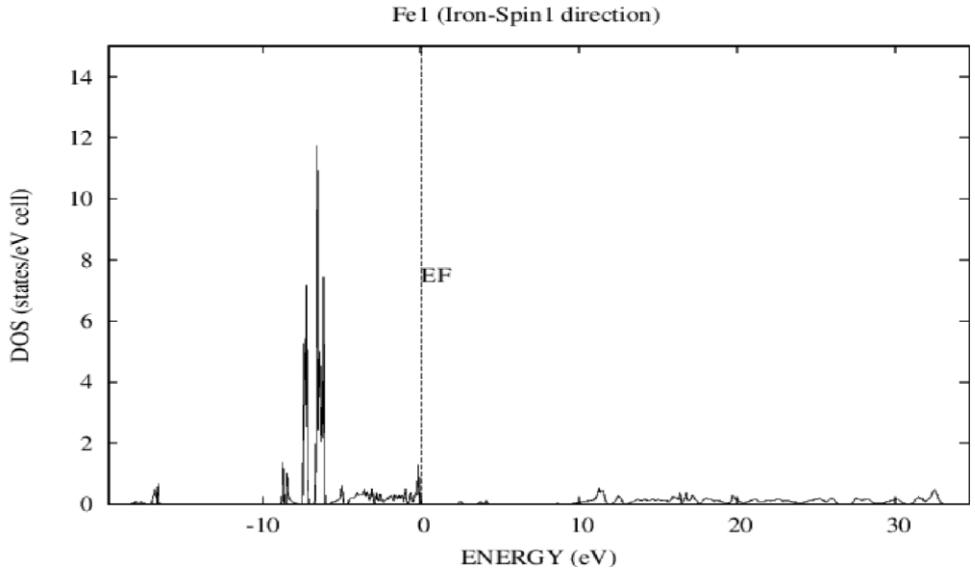

Fig. 6.10: Partial density of states plot for Fe1 atom in spin-1 direction

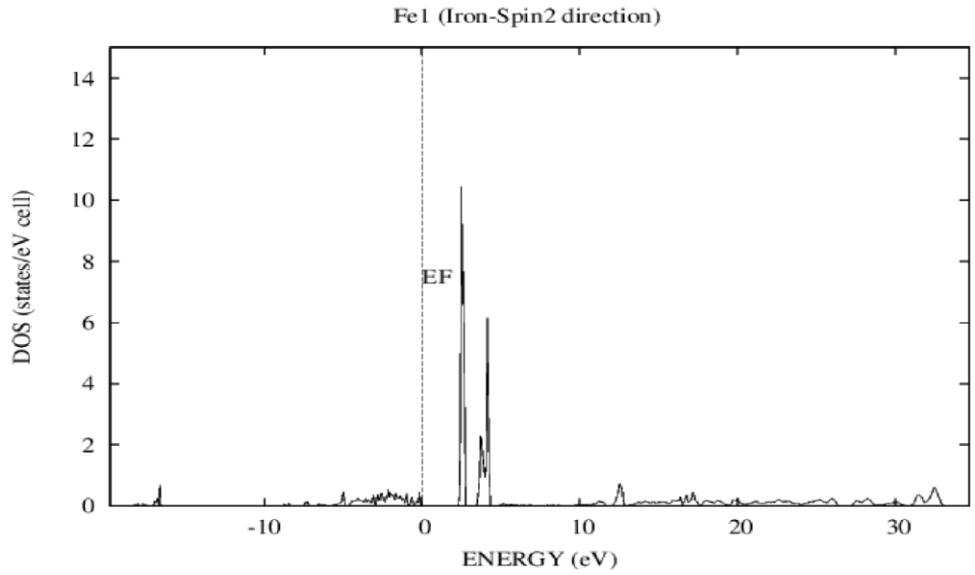

Fig. 6.11 Partial density of states plot for Fe1 atom in spin-2 direction

:

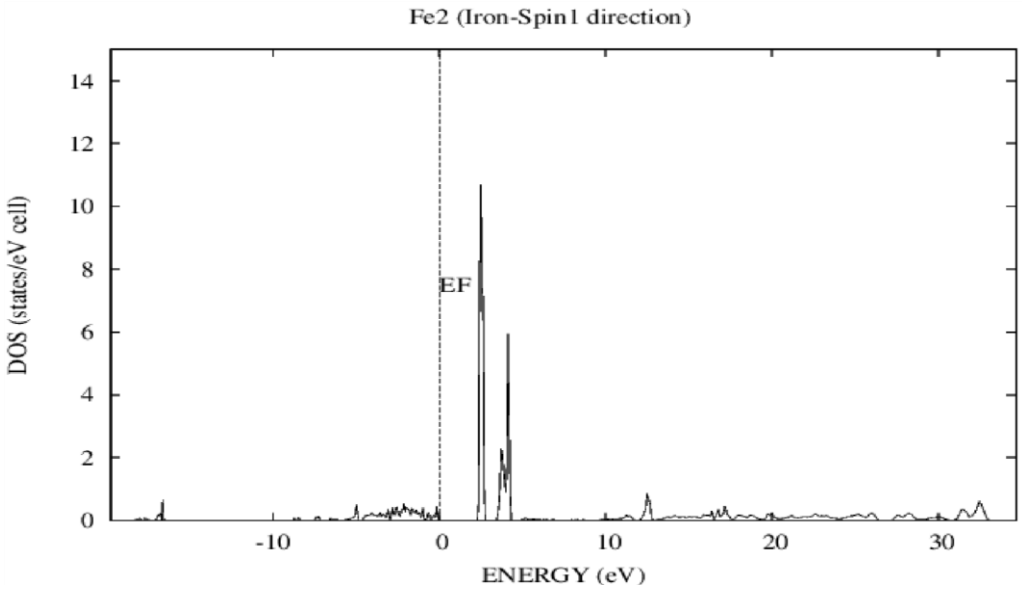

Fig. 6.12: Partial density of states plot for Fe2 atom in spin-1 direction

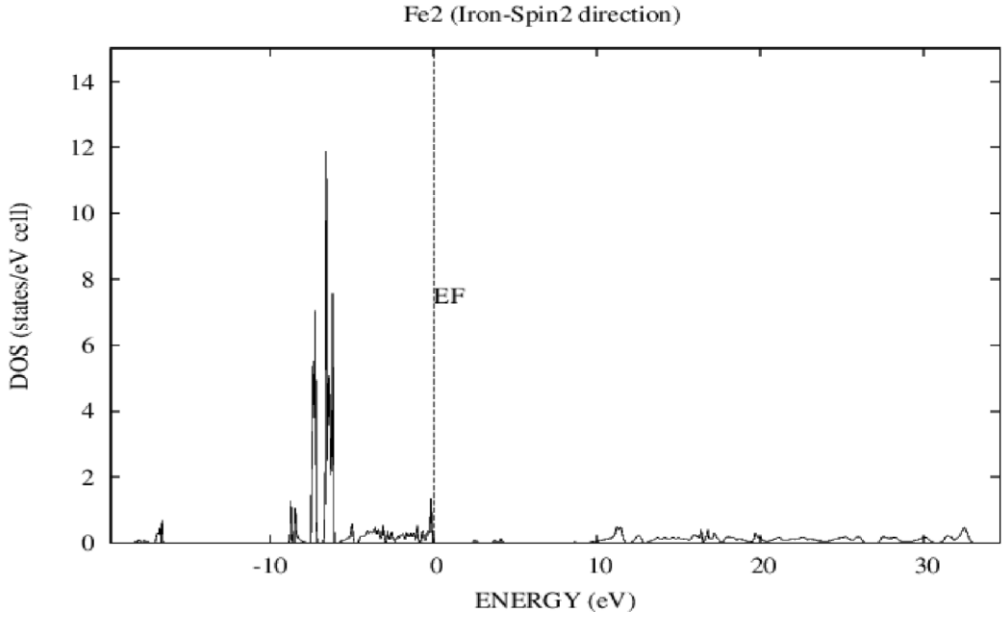

Fig. 6.13 Partial density of states plot for Fe2 atom in spin-2 direction

:

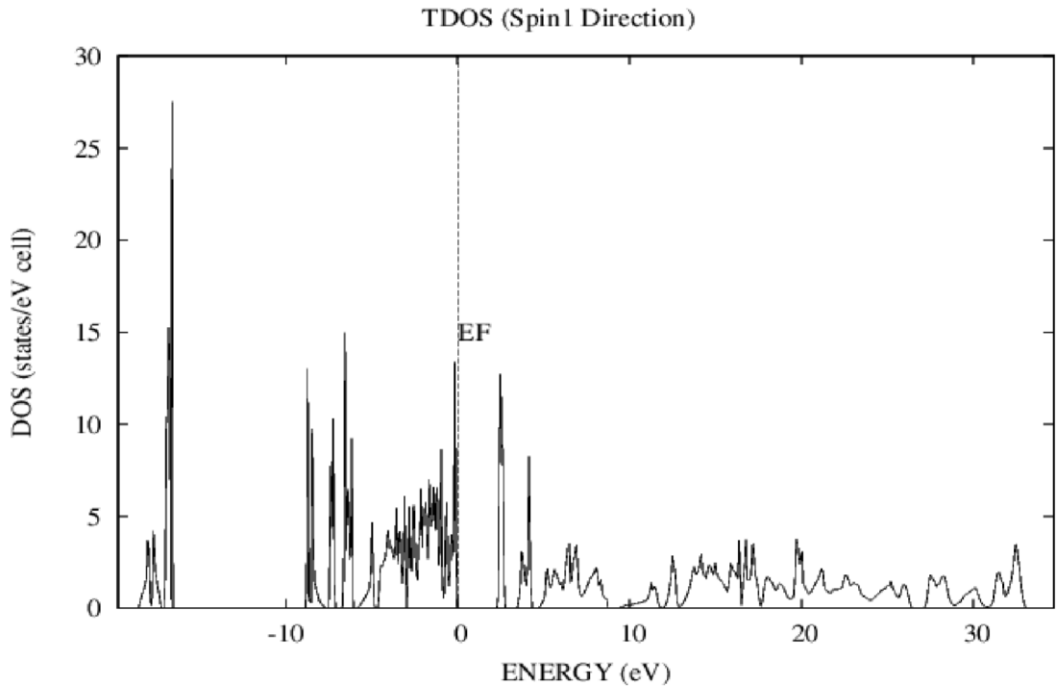

Fig. 6.14: Total density of states plot in spin-1 direction

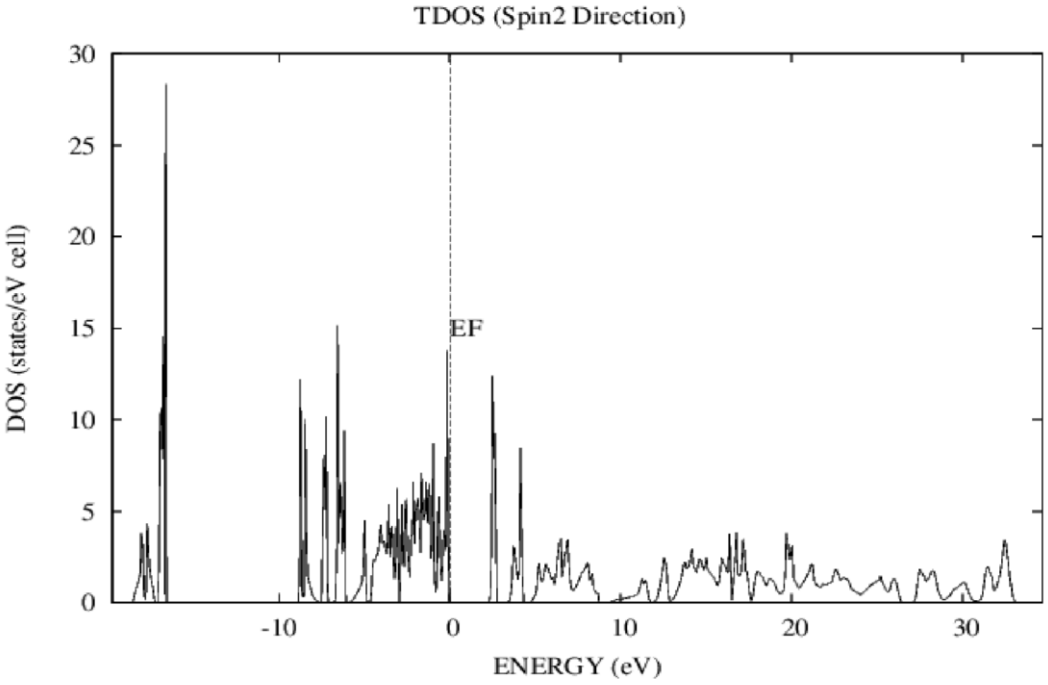

Fig. 6.15: Total density of states plot in spin-2 direction

From figs-6.6, 6.7, 6.8, and 6.9 it was observed that the partial density of states plots for both Bismuth (Bi) and oxygen (O) have identical density of states plots in spin-1 and spin-2 directions. However from Figs-6.10, 6.11, 6.12 and 6.13 it was observed that the partial density of states plot were quite different for Fe1 and Fe2 in the two spin directions (spin-1 and spin-2) thereby indicating the anti-ferromagnetic behavior [26]. Also it was observed that the total density of states plots in spin-1 and spin-2 directions as shown in Figs-6.14 and 6.15 are identical thereby showing the anti-ferromagnetic ordering in the ground state $BiFeO_3$ [25, 26]. However slight differences were observed from the exactly identical expected density of states plots in Figs-6.14 and 6.14. It was concluded that the reason for this small amount of error is due to the numerical errors in the SCF calculations due to the low symmetry inherited in the calculation because of the introduction of empty spheres in the TB-LMTO-ASA methodology for carrying out the SCF calculations.

6.3 Electronic and magnetic properties of a pure ground state $BiFeO_3$ calcined at 600^0C

Next in order to calculate the electronic and magnetic properties of $BiFeO_3$ calcined at 600 °C, the lattice parameters and the fractional coordinates of the atoms were used as shown below in the table 6.2.

Table 6.2: Fractional coordinates and the lattice parameters of ground state $BiFeO_3$ calcined at 600 °C

Composition $BiFeO_3$	Atom	Fractional Co-ordinates			Lattice Constant (Å)	Band Gap (eV)
		x	y	z		
At 600 ^{0}C Space Group: R3c	Bi	0	0	0.00593	a = 5.573095, c = 13.846117	2.09
	Fe	0	0	0.22855		
	O	0.45678	0.01654	-0.0565		

Further in order to check the effect of calcination temperatures on the band gap and magnetic ordering of ground state $BiFeO_3$, same combination of Hubbard parameters U = 6eV and J = 1eV (i.e. U_{eff} = 5eV) were used to perform the SCF calculations as were used for performing the SCF

calculations for the previous first sample calcined at 500°C. In order to extract the nature of band gap and the type of magnetic ordering in ground state $BiFeO_3$ calcined at 600 °C the energy band structure diagrams were obtained in the spin-1 and spin-2 directions as shown below in Fig.6.16 and 6.17 respectively. From Fig.6.16 and 6.17 it was observed that the ground state $BiFeO_3$ calcined at 600°C also possess a direct band gap which is in agreement with that observed experimentally [58]. Also it was observed that the energy band structure diagrams are identical in the two spin directions (spin-1 and spin-2) indicating again the anti-ferromagnetic behaviour in ground state $BiFeO_3$ calcined at 600°C [25, 26].

Next in order to extract the energy band gap value the total density of states plot was obtained as shown below in Fig-6.18. From the Fig-6.18 an electronic band gap of 2.16 eV was observed which is close to that obtained from the experiments i.e 2.04 eV as given in the Table 6.1 [58] with the value of magnetic moment on Fe atoms of ~ 4.06 $\mu_{B.}$ Lastly in order to further authenticate the antiferromagnetic ordering in ground state $BiFeO_3$ calcined at 600°C, the partial density of states plots for Bismuth (Bi), Oxygen (O), Iron (Fe1) and Iron (Fe2) along with TDOS were obtained in the spin1 and spin2 directions as shown below in Fig 6.19, 6.20, 6.21, 6.22, 6.23, 6.24, 6.25, 6.26, 6.27 and 6.28. Again from these figures it was observed that the PDOS for Bismuth and Oxygen and TDOS's are identical in the two spin directions (Spin1 and 2) whereas the PDOS are different for Fe1 and Fe2 in the two spin directions (spin1 and 2) thereby again confirming the antiferromagnetic ordering in ground state $BiFeO_3$ calcined at 600°C.

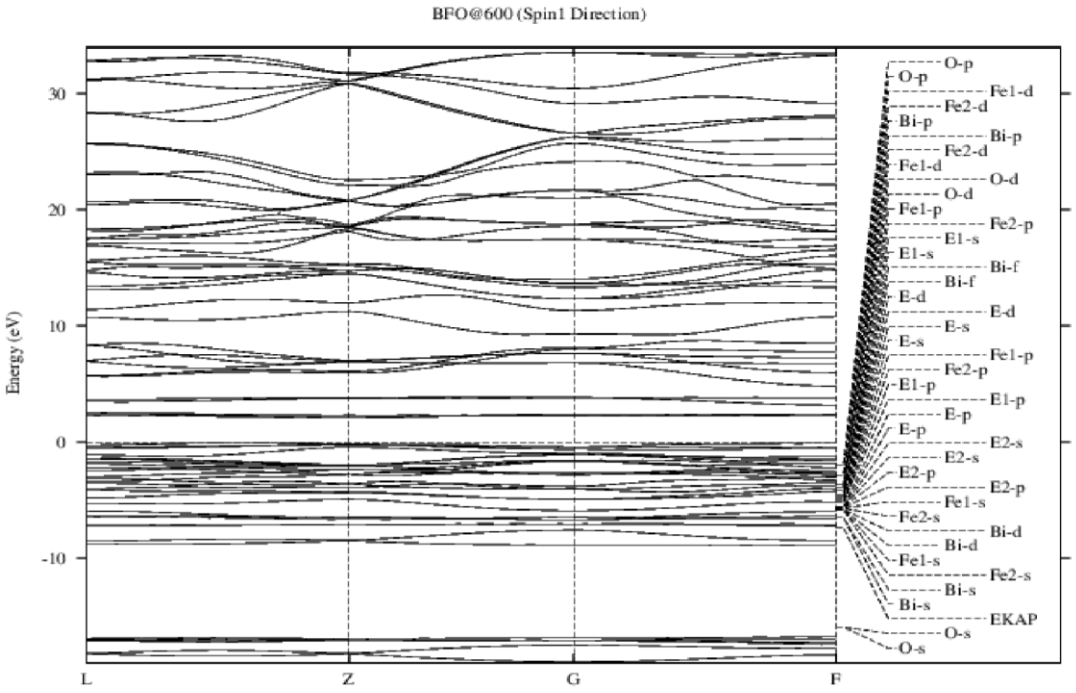

Fig. 6.16: Energy band structure diagram in spin-1 direction

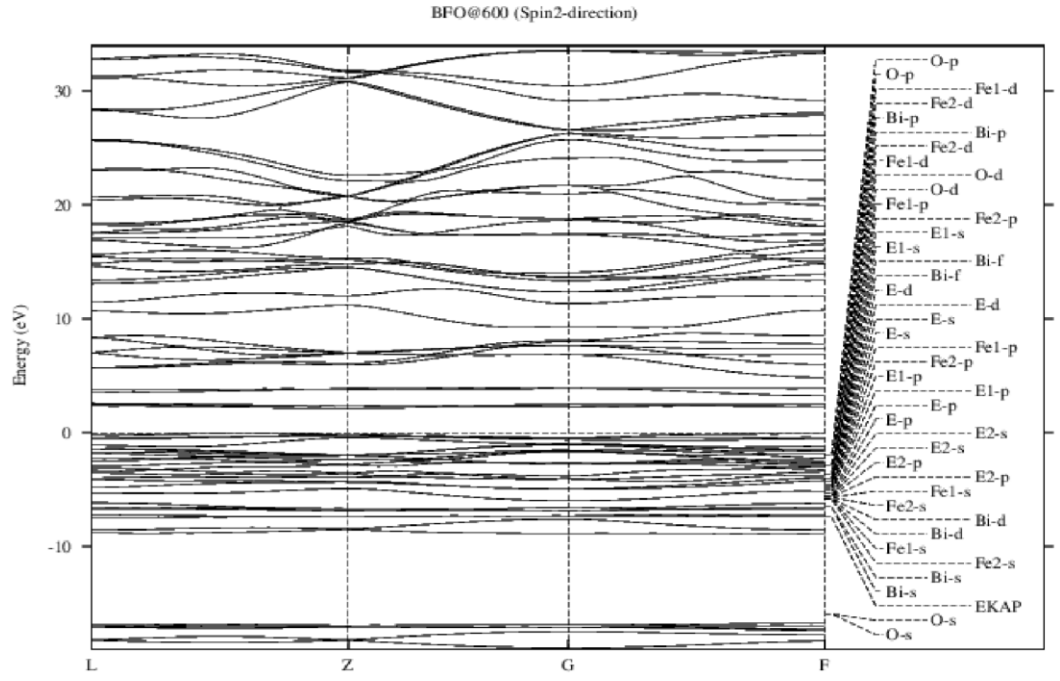

Fig. 6.17: Energy band structure diagram in spin-2 direction

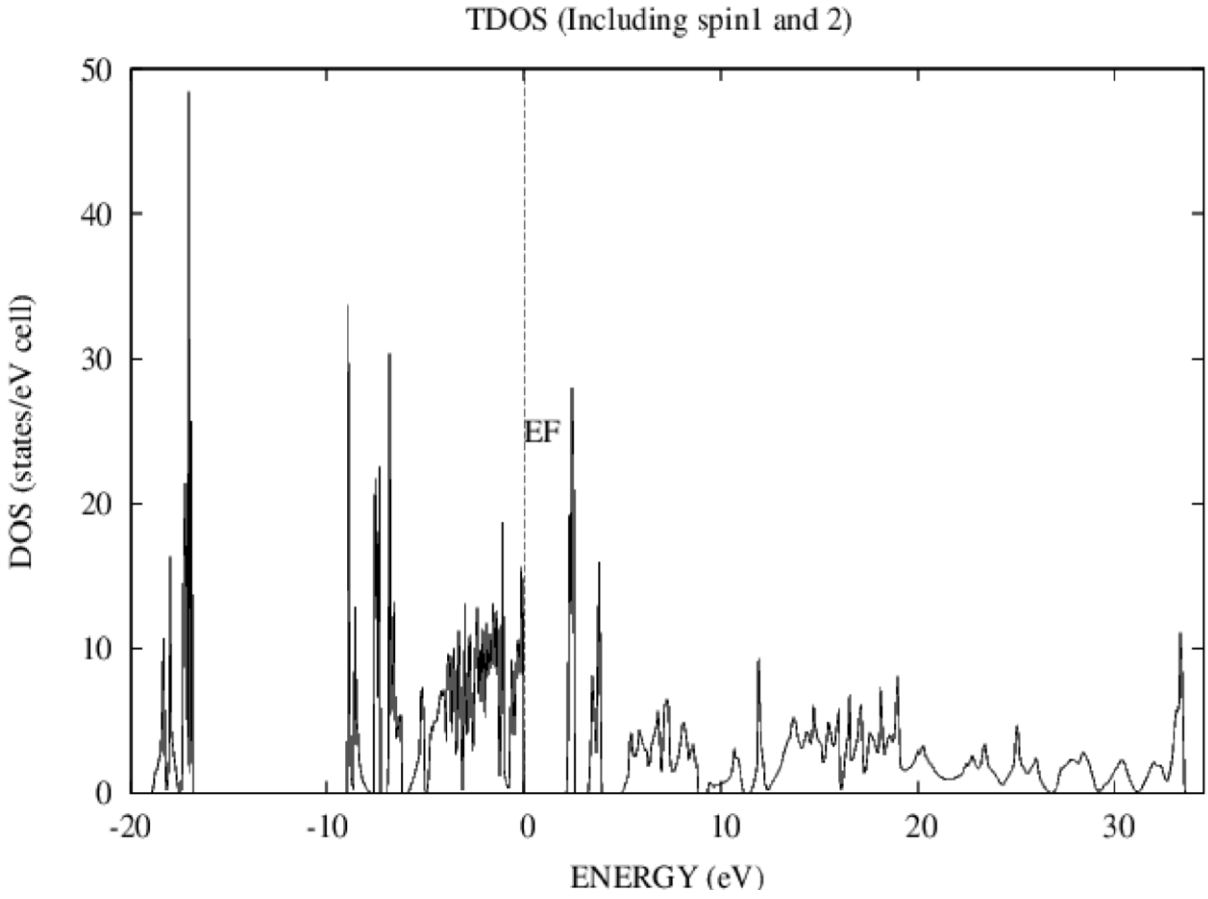

Fig. 6.18: Total density of states plot including contributions from both spin-1 and spin-2 directions

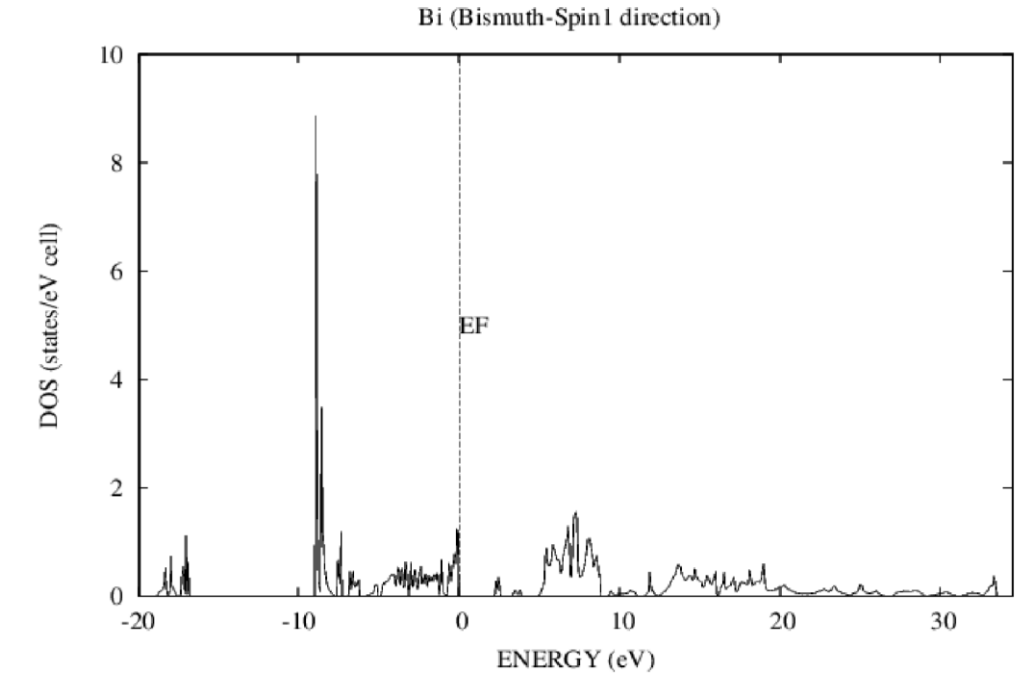

Fig. 6.19: Partial density of states plot for Bi (Bismuth) in spin-1 direction

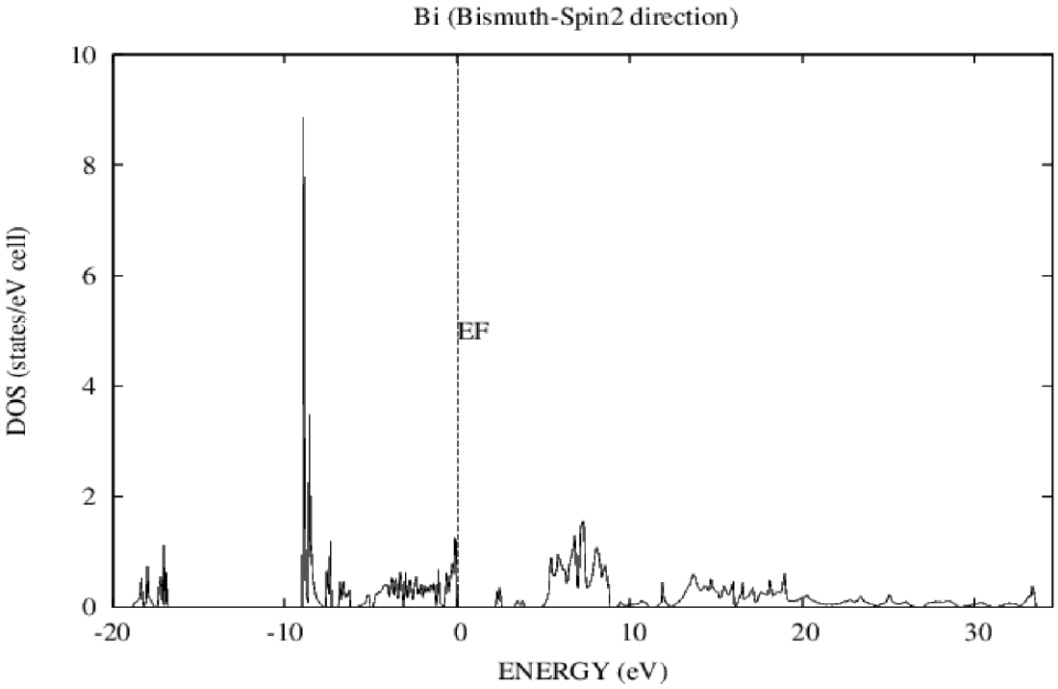

Fig. 6.20: Partial density of states plot for Bi (Bismuth) in spin-2 direction

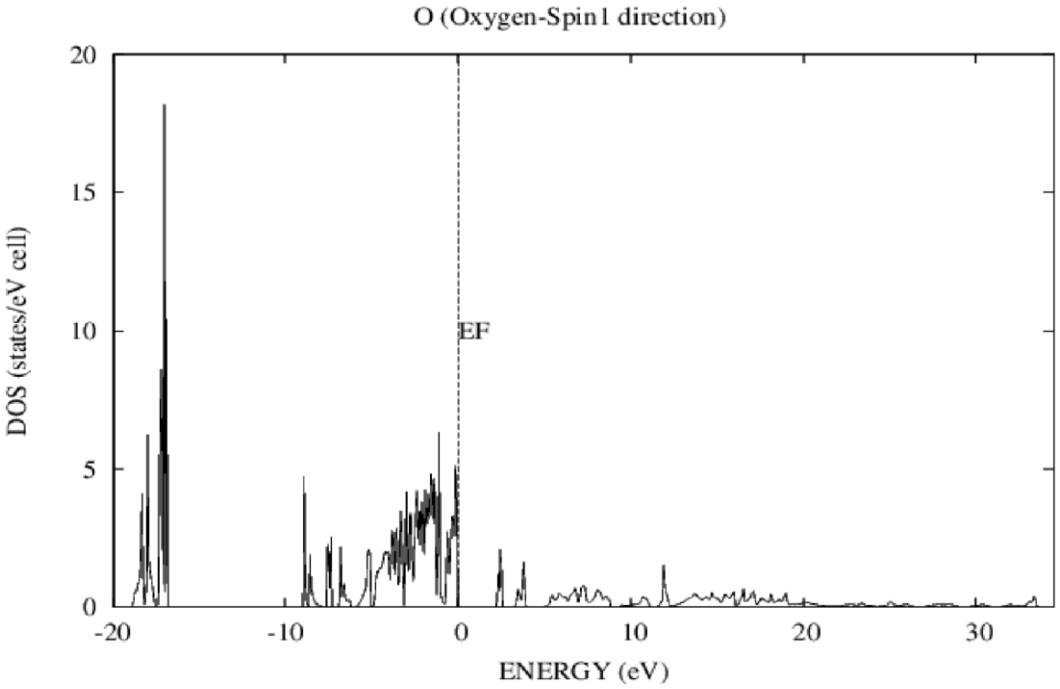

Fig. 6.21: Partial density of states plot for O (Oxygen) in spin1 direction

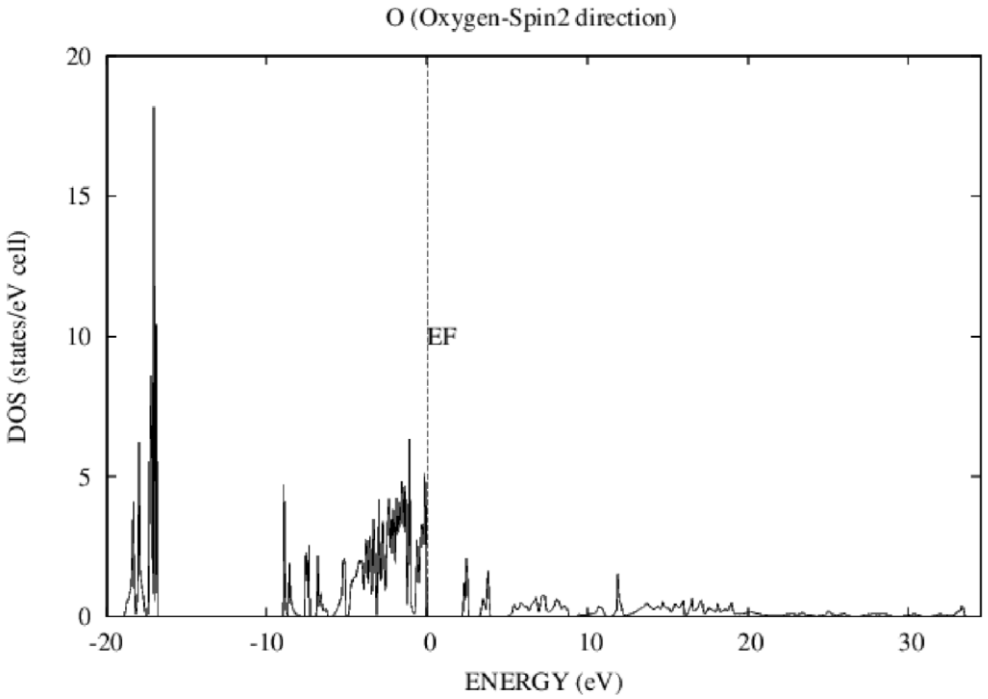

Fig 6. 22: Partial density of states plot for O (Oxygen) in spin2 direction

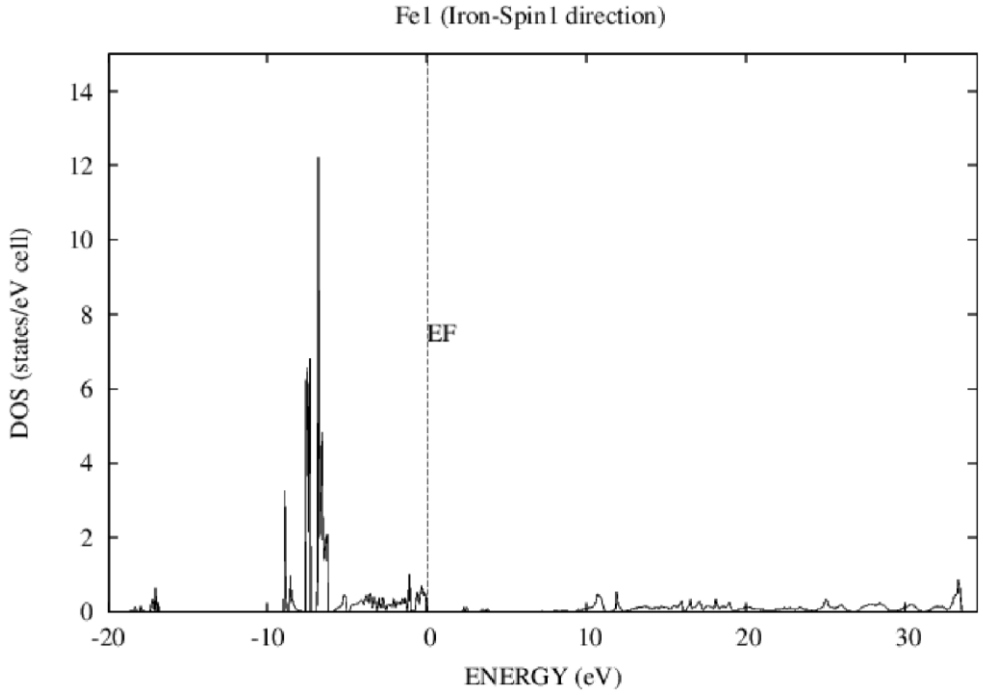

Fig. 6.23: Partial density of states plot for Iron (Fe1) in spin-1 direction

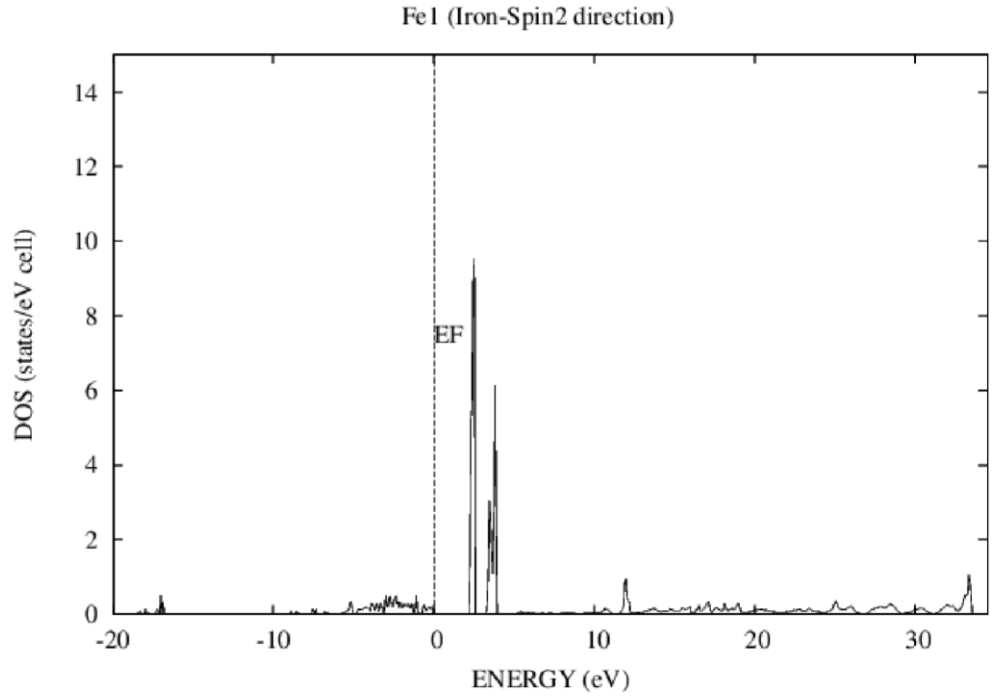

Fig. 6.24: Partial density of states plot for Iron (Fe1) in spin-2 direction

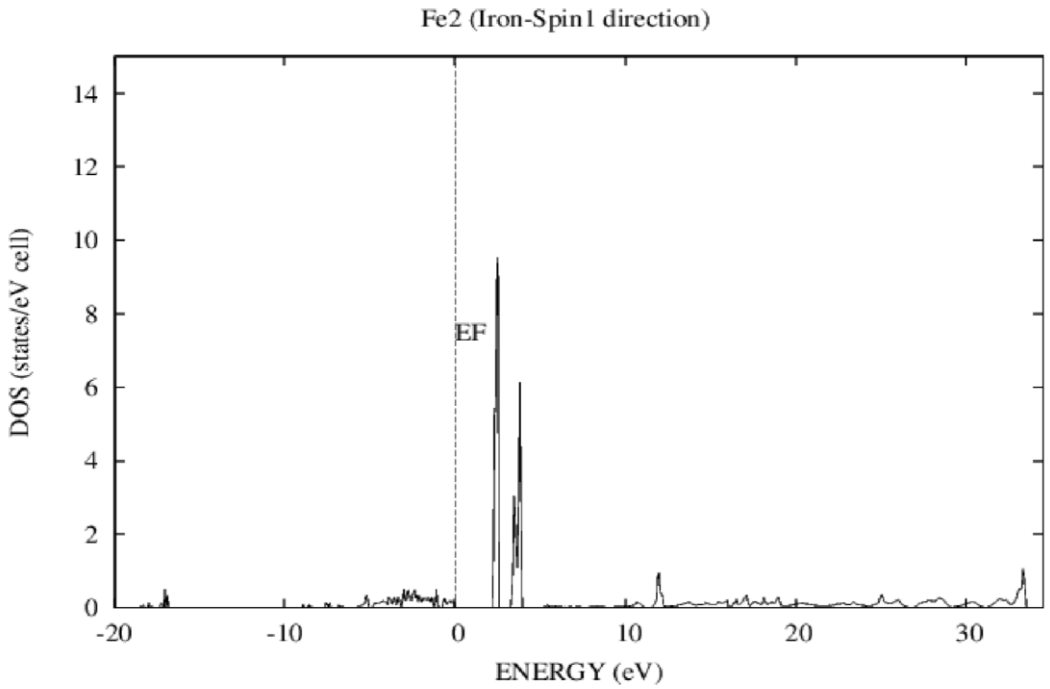

Fig. 6.25: Partial density of states plot for Iron (Fe2) in spin-1 direction

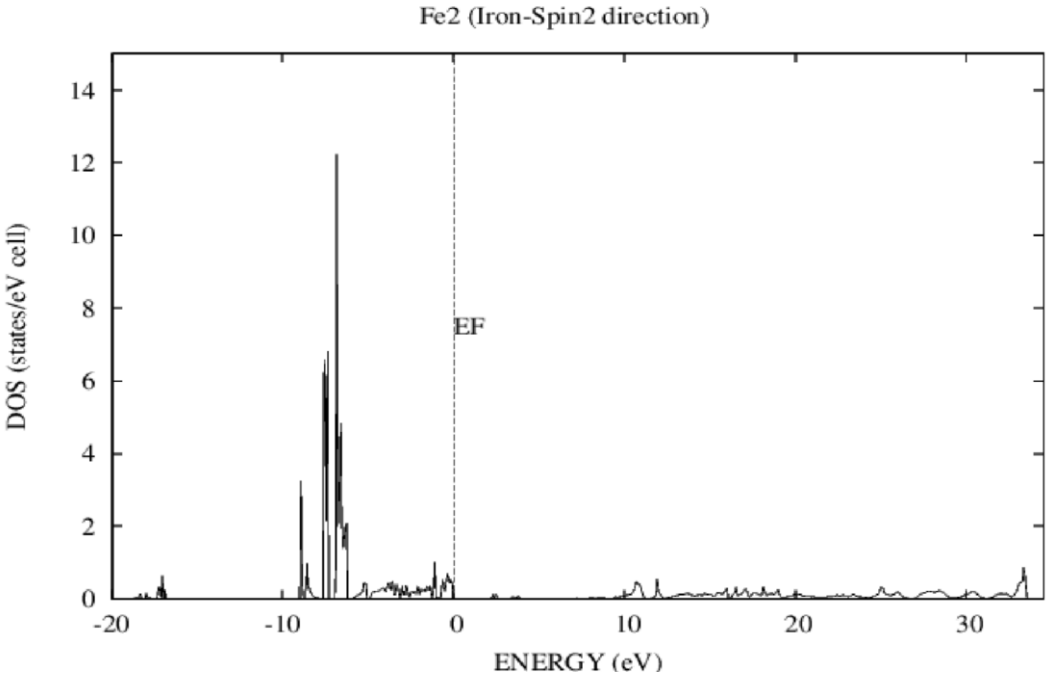

Fig. 6.26: Partial density of states plot for Iron (Fe2) in spin-2 direction

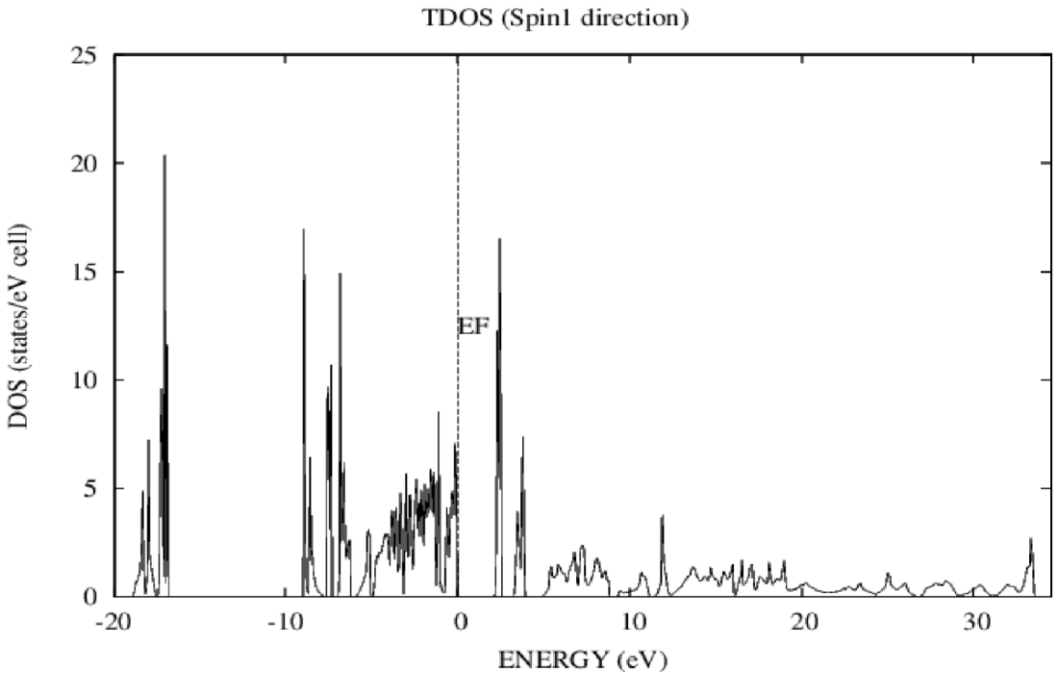

Fig. 6.27: Total density of states plot in spin-1 direction

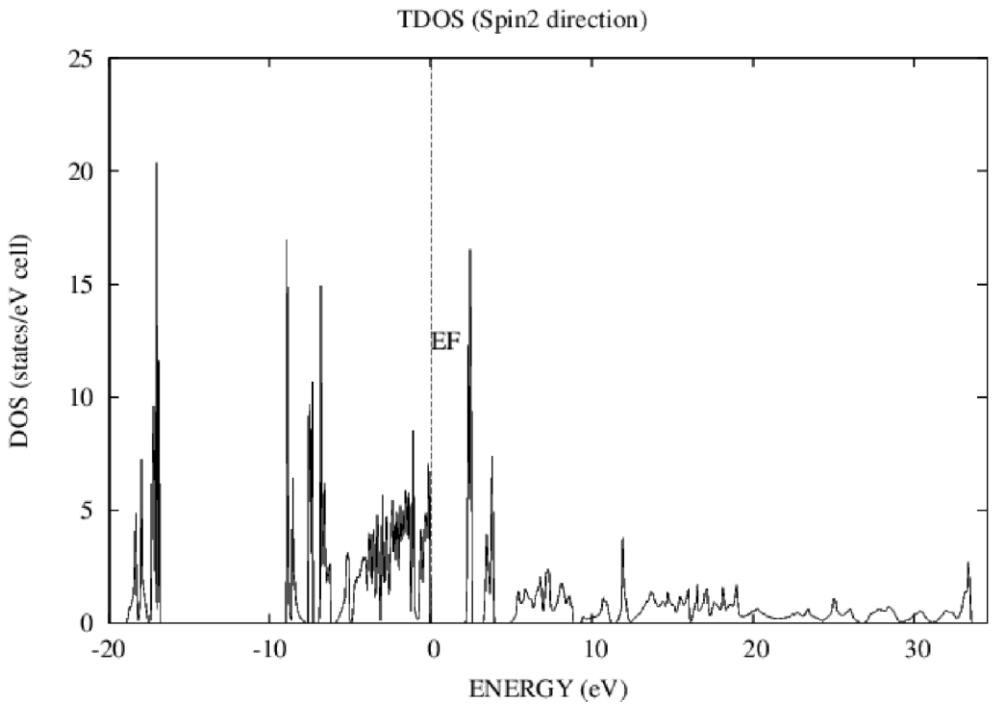

Fig. 6.28: Total density of states plot in spin-2 direction

6.4 Charge density analysis of ground state $BiFeO_3$ calcined at 500 and 600 ° C

In order to study the nature of chemical bonding between the atoms of $BiFeO_3$ a charge density plots identical for both 500°C and 600°C in 2 and 3 dimensions were obtained in a plane as shown below in Fig 6.29 and 6.30. From Fig 6.29 and 6.30 it was observed that the chemical bonding between Fe and O is not completely ionic due to the presence of finite amount of directional covalent bonding. This directional covalent bonding is indicated by the directional nature of the charge distribution between the Fe and O atoms. Since the ferroelectricity is impossible in $BiFeO_3$ if the chemical bonding between its atoms is purely ionic leading to centrosymmetric setup. Hence the existence of ferroelectricity was observed due to the presence of finite amount of covalent bonding between the constituent atoms of $BiFeO_3$ leading to non-Centro symmetric setup [47].

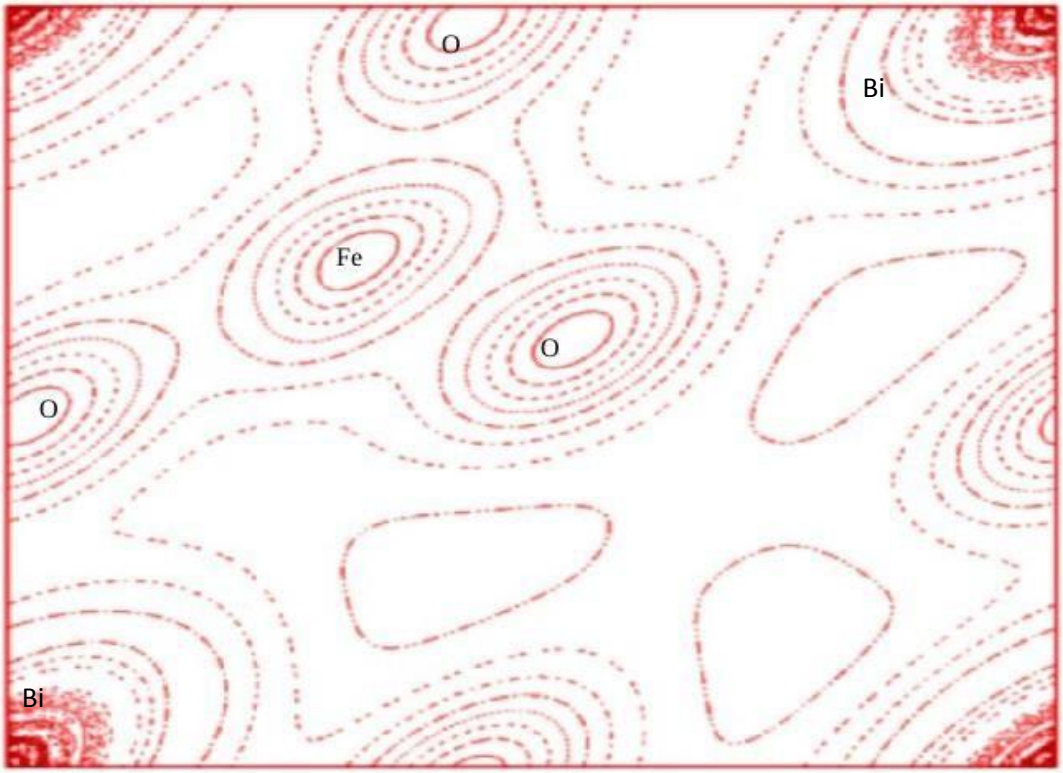

Fig. 6.29: Charge density plot for $BiFeO_3$ in 2 dimensions

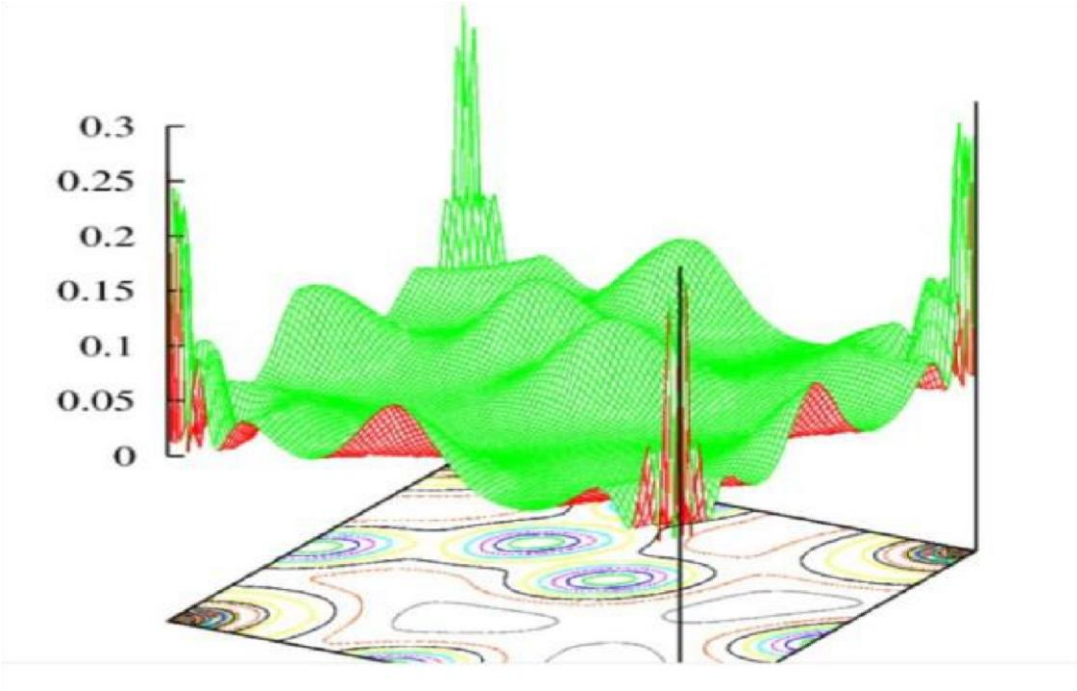

Fig. 6.30: Charge density plot for $BiFeO_3$ in 3 dimensions

6.5 Comparison of theoretical band gaps obtained for $BiFeO_3$ at 500 °C and 600 °C with that obtained from the experiments

From table-6.3 below, it was observed that the theoretical band gap values decreased with the increase in temperature in accord with the the observation obtained from the experiments.

Table 6.3: Comparison of theoretically obtained band gaps at different calcination temperatures of $BiFeO_3$

Temperature of calcination of $BiFeO_3$	**Experimentally obatained value of band gap (in eV)**	**Theoretically obtained value of band gap (in eV) using U_{eff} = 5 eV i.e U = 6 eV & J = 1 eV**
500^0C	2.16 eV	2.25 eV
600^0C	2.04 eV	2.16 eV

Conclusions and Future scope

From the results and their discussions in chapter 6, following conclusions can be made;

1. DFT calculations performed using GGA+U methodology under TB-LMTO-ASA code version 47 [61, 62] predicted accurately the electronic properties of ground state $BiFeO_3$ based on its hexagonal 10 atoms unit cell.

2. Value of the effective Hubbard parameter U_{eff} = 5 eV (U = 6 eV and J = 1 eV) implemented in GGA+U scheme under the DFT frame to perform the SCF calculations gave the correct estimates for the energy band gaps of ground state rhombohedral (R3c) phase $BiFeO_3$ with slight overestimations of the magnetic moment on Fe atoms in $BiFeO_3$ whereas the value of effective Hubbard parameter U_{eff} = 0.5 eV (U = 1.5 eV and J = 1eV) gave the correct estimate for the magnetic moment on Fe atoms of ~ 3.73 μ_B in $BiFeO_3$ in exact agreement with that observed experimentally.

3. It was observed from our theoretical calculations that the energy band gap decreased with the increase in calcination temperature of pure ground state $BiFeO_3$ samples which agree well with the experimental findings.

4. Direct band gaps were observed theoretically from the energy band structure diagrams for both the samples calcined at 500^0C and 600^0C which was also observed experimentally.

5. Directional covalent bonding was observed in addition to ionic bonding in the charge density plot thereby indicating the non-centrosymmetric setup causing ferroelectricity.

Future scope

DFT studies using the TB-LMTO-ASA code could be done to study the doped $BiFeO_3$ systems and the effect of dopants (La, Sr etc.) on the energy band gap of the doped $BiFeO_3$ system can be found effectively.

References

1. H. Schmid, Ferroelectrics 162, 317–338 (1994)
2. M. Dawber, K. M. Rabe, and J. F. Scott, Rev. Mod. Phys. 77, 1083 (2005)
3. J. F. Scott, J. Phys. Cond. Matter 20, 021001 (2000)
4. D. Khomskii, Classifying multiferroics: mechanisms and effects, Physics,V. 2, p.20, (2009)
5. Y.H. Chu, L.W. Martin, M.B. Holcomb and Ramesh, Ramamoorthy, Materials Today 10, 16–23 (2007)
6. B.B. Van Aken, T.T.M. Palstra, A. Filippetti and N.A. Spaldin, Nat. Mater. 3, 164 (2004)
7. J.B. Goodenough and J.M. Longo, Landolt-Bornstein, Numerical Data and Functional Relationships in Sciesnce and Technology, New Series Vol.III.4, 126, Springer, Berlin, (1970)
8. T. Mitsui, Landolt-Bornstein, Numerical data and Functional Relations in Science and Technology, New Series Vol. 16, No. 1, Springer,Berlin, (1981)
9. S.W. Cheong and M. Mostovoy, Nature Materials 6, 13 (2007)
10. Special issue," Special Sections Containing Papers on Multiferroics and On Multiferroics and Manganites", J. Phys. Condens. Matter. 20, 434201–434220 (2008)
11. B.B. VanAken, T.T.M. Palstra, A. Filippetti and N.A. Spaldin, Nature Mater. 3, 164 (2004)
12. T. Kimura, T. Goto, H. Shintani, K. Ishizaka, T. Arima and Y.Tokura, Nature 426, 55 (2003)
13. N. Hur, S. Park, P.A. Sharma, J. S. Ahn, S. Guha and S.W. Cheong, Nature 429, 392 (2004)
14. Y.J. Choi, H.T. YI, S. Lee, Q. Huang, V. Kiryukhin and S.W. Cheong, Phys. Rev. Lett. 100, 047601 (2008)
15. J. Wang, J. B. Neaton, H. Zheng, V. Nagarajan, S. B. Ogale, B. Liu, D. Viehland, V. Vaithyanathan, D. G. Schlom, U. V. Waghmare, N. A. Spaldin, K. M. Rabe, M. Wuttig, and R. Ramesh, Science 299, 1719 (2003)
16. C. Michel, J.M. Moreau, G.D. Achenbach, R. Gerson, and W.J. James, Solid State Communications 7, 701 (1969)
17. J.M. Moreau, C. Michel, R. Gerson and W.J. James, J. Phys. Chem. Solid. 32, 1315 (1971)
18. G. Catalan and J.F. Scott, Advanced Materials 21, 2463 (2009)

19. D. Lebeugle, D. Colson, A. Forget and M. Viret, Appl. Phys. Lett. 91, 022907 (2007)
20. V.V. Shvartsman, W. Kleeman, R. Haumont and J. Kreisel, Appl. Phys. Lett. 90, 172115 (2007)
21. D. Lebeugle, D. Colson, A. Forget, M. Viret, P. Bonville, J. F. Marucco, and S. Fusil, Phys. Rev. B 76, 024116 (2007)
22. S. V. Kiselev, R. P. Ozerov and G. S. Zhdanov, Sov. Phys. Dokl. 7, 742 (1963)
23. Sosnowska, T. Peterlin-Neumaier and E. Steichele, J. Phys. C: solid State Phys. 15, 4835 (1982)
24. Sosnowska, M. Loewenhaupt, W. I. F. Davie and R. M. Ibberson, Physica B, 180-181, 117 (1992)
25. H. Wang, Y. Zheng, M.Q. Cai and H. Huang, Solid state Communications, 149, 641-644 (2009)
26. Q. Li, D.H. Huang, Q.L. Cao and F.H. Wang, Chin. Phys. B 22, 037101, (2013)
27. F. Gao, Y. Yuan, K.F. Wang, X.Y. Chen, F. Chen, J.M. Liu and Z.F. Ren, Appl. Phys. Lett. 89, 102506 (2006)
28. Sosnowska, R. Przeniosło, P. Fischer and V.A. Murashov, Acta Physica Polonica A 86, 4 (1994)
29. L. Fei, Y. Hu, X. Li, R. Song, S. Li, H. Huang, H. Gu, H.L.W. Chan and W. Yu, Appl. Mater. Interfaces 7, 3665−3670 (2015)
30. G.G. Khan, R. Das, N. Mukherjee and K. Mandal, Phys. Status Solidi RRL 6, 312–314 (2012)
31. D.K. Mishra and X. Qi, Journal of Alloys and Compounds 504, 27–31 (2010)
32. P. Hohenberg and W. Kohn, Phys. Rev. 136, B864 (1964)
33. M. Born and R. Oppenheimer, Annalen der Physik 84, 457 (1927)
34. W. Kohn and L.J. Sham, Phys. Rev. 140, A1133 (1965)
35. R.O. Jones and O. Gunnarsson, Rev. Mod. Phys. 61, 689 (1989)
36. S.H. Vosko, L. Wilk and M. Nusair, Can. J. Phys. 58, 1200 (1980)
37. J.P. Perdew and A. Zunger, Phys. Rev. B 23, 5048 (1981)
38. L.A. Cole and J.P. Perdew, Phys. Rev. A 25, 1265 (1982)
39. J.P. Perdew and Y. Wang, Phys. Rev. B 45, 13244 (1992)
40. A.D. Becke, Phys. Rev. A 38, 3098 (1988)

41. J.P. Perdew, J.A. Chevary, S.H. Vosko, K.A. Jackson, M.R. Pederson, and C. Fiolhais, Phys. Rev. B 46, 6671 (1992)

42. J.P. Perdew, K. Burke, and M. Ernzerhof, Phys. Rev. Lett. 77, 3865 (1996)
43. V.I. Anisimov, F. Aryasetiawan and A.I. Lichtenstein, J. Phys. Condens. Matter 9, 767 (1997)

44. J. B. Neaton, C. Ederer, U. V. Waghmare, N. A. Spaldin, and K. M. Rabe, Phys. Rev. B 71, 014113 (2005)

45. F. Kubel and H. Schmid, Acta Crystallogr. Sect. B: Struct. Sci. 46, 698 (1990)
46. I. Sosnowska, W. Schäfer, W. Kockelmann, K.H. Andersen and I.O. Troyanchuk, Appl. Phys. A: Mater. Sci. Process. 74, S1040 (2002)

47. P. Ravindran, R. Vidya, A. Kjekshus, H. Fjellvåg, and O. Eriksson, Phys. Rev. B 74, 224412, (2006)

48. S.J. Clark and J. Robertson, Appl. Phys. Lett. 90, 132903 (2007)

49. S. Ju, T.Y. Cai, G.Y. Guo, The Journal of Chemical Physics 130, 214708 (2009)

50. Y. Wang, J.E. Saal, P. Wu, J. Wang, S. Shang, Z.K. Liu, L.Q. Chen, Acta Materialia 59, 4229–4234 (2011)

51. J. Kaczkowski, M. Pugaczowa-Michalska, A. Jezierski, Acta Physica Polonica A 127, 266 (2015)

52. P. Singh, A. Roy, A. Garg and R. Prasad, Journal of Applied Physics 117, 184104 (2015)

53. R. Palai, R.S. Katiyar, H. Schmid, P. Tissot, S.J. Clark, J. Robertson, S.A.T. Redfern, G. Catalan and J.F. Scott, Phys. Rev. B 77, 014110 (2008)

54. O.K. Andersen and O. Jepsen, Phys. Rev. Lett. 53, 2571 (1984)

55. O.K. Andersen, Z. Pawlowska, and O. Jepsen, Phys. Rev. B 34, 5253 (1986)

56. H.J. Monkhorst and J.D. Pack, Phys. Rev. B 13, 5188 (1976)

57. P.E. Blöchl, O. Jepsen, and O.K. Andersen, Phys. Rev. B 49, 16 223, (1994)

58. M. Kaur, K.L. Yadav and P. Uniyal, Advanced Materials Letters (Accepted)